

1 **Interseismic Strain Accumulation across the Main**  
2 **Recent Fault, SW Iran, from Sentinel-1 InSAR**  
3 **Observations**

4 **Andrew R. Watson<sup>1</sup>, John R. Elliott<sup>1</sup>, Richard J. Walters<sup>2</sup>**

5 <sup>1</sup>COMET, School of Earth and Environment, University of Leeds, UK

6 <sup>2</sup>COMET, Department of Earth Sciences, Durham University, UK

7 **Key Points:**

- 8 • We derive East and Vertical surface velocities from 5.5 years of Sentinel-1 synthetic  
9 aperture radar images over the western Zagros.
- 10 • We estimate an interseismic slip rate of  $3.0 \pm 1.0$  mm/yr ( $2\sigma$ ) for the Main Re-  
11 cent Fault, in agreement with previous GNSS studies.
- 12 • We estimate a geodetically-determined interseismic locking depth of 18–30 km,  
13 a first for this fault.

## Abstract

The Main Recent Fault is a major right-lateral strike-slip fault in the western Zagros mountains of Iran. Previous studies have estimated a wide range of slip rates from both sparse GNSS (1–6 mm/yr) and geological/geomorphological (1.6–17 mm/yr) methods. None of these studies have estimated the depth to the top of the locked seismogenic zone. Characterizing this "locking depth" for the Main Recent Fault, and more accurately constraining its interseismic slip rate, are both critical for estimating the seismic hazard posed by the fault, as well as for understanding how oblique convergence is accommodated and partitioned across the Zagros. To address this important knowledge gap for the MRF, here we use 200 Sentinel-1 SAR images from the past 5 years, spanning two ascending and two descending tracks, to estimate the first InSAR-derived slip rate and locking depth for a 300 km long section of the fault. We utilise two established processing systems, LiCSAR and LiCSBAS, to produce interferograms and perform time series analysis, respectively. We constrain north-south motion using GNSS observations, decompose our InSAR line-of-sight velocities into fault-parallel and vertical motion, and fit 1-D screw dislocation models to three fault-perpendicular profiles of fault-parallel velocity, following a Bayesian approach to estimate the posterior probability distribution on the fault parameters. We estimate an interseismic slip velocity of  $3.0 \pm 1.0$  mm/yr below a loosely constrained 18–30 km locking depth, the first such estimate for the fault, and discuss the challenges in constraining the locking depth for low magnitude interseismic signals.

## Plain Language Summary

Convergence between the Arabian and Eurasian plates is causing deformation of the Earth's crust in Iran. Some of this motion is taken up by movement at depth on the Main Recent Fault, which is stuck by friction near the Earth's surface and is therefore accumulating strain which may then be released in an earthquake. We use five years of satellite radar images to measure the average velocity of the ground surface either side of the fault. By looking at the velocity difference across the fault, along with the gradient, we can estimate the rate at which the fault is accumulating strain and the depth below which this is occurring. Our estimated rate of  $3.0 \pm 1.0$  mm/yr is in agreement with previous estimates from GPS studies, while our estimate of the locking depth, from 18–30 km, is the first such estimate for the fault. The broad range of possible values for the locking depth highlights the difficulties of studying tectonic signals when they are close in magnitude to the sensing limit of our satellite imagery method (1 mm/yr).

## 1 Introduction

The Main Recent Fault (MRF) is a 800 km long dextral strike-slip fault in the hinterlands of the Zagros mountains, Iran. The fault is one of the most seismically active in the northwestern Zagros, having experienced historical earthquakes up to  $M_s$  7.4 (Ambraseys & Moinfar, 1973; Ghods et al., 2012; Karasózen et al., 2019), driven by convergence between the Arabian and Eurasian plates. During the interseismic period of the earthquake cycle, the MRF can be viewed as accumulating strain in the locked upper crust whilst slipping aseismically at depth, following that assumed for other strike-slip fault zones (Savage & Prescott, 1978; Thatcher, 1983; Savage, 2000; Wright et al., 2013). Estimates of interseismic slip rate and the depth-extent of the locked seismogenic zone, from here on referred to as the 'locking depth', are critical to our understanding of both the local seismic hazard (Smith-Konter & Sandwell, 2009), and the accommodation of oblique convergence across the Zagros. Despite the importance of the MRF for understanding Iranian tectonics and seismic hazard, its interseismic slip rate is still poorly constrained, and no estimates for the locking depth of the fault have been published. Previous studies of the MRF have used a range of geological markers, geomorphological offsets, cosmogenic isotope dating, and Global Navigation Satellite System (GNSS) measurements

64 to estimate a wide range (1–17 mm/yr) of possible slip rates (Table 1). The average slip  
 65 rates determined from long-term geological/geomorphological offsets (1.6–17 mm/yr, Talebian  
 66 & Jackson, 2002; Bachmanov et al., 2004; Copley & Jackson, 2006; Alipoor et al., 2012)  
 67 and cosmogenic dating (3.5–12.5 mm/yr, Authemayou et al., 2009) cover a broader range  
 68 with higher upper bounds than geodetic slip rates from decadal GNSS studies (1–7 mm/yr,  
 69 Vernant et al., 2004; Hessami et al., 2006; Walpersdorf et al., 2006; Khorrami et al., 2019).  
 70 The large variation in geological and geomorphological slip rates reflects differences in  
 71 the time scales of the estimates (thousands vs. millions of years), uncertainties in the  
 72 measured offsets, and uncertainties in the age of the MRF. Meanwhile, GNSS-derived  
 73 estimates have suffered from the sparsity of instruments in Iran, especially in the south  
 74 west and in northern Iraq.

75 Interferometric Synthetic Aperture Radar (InSAR) time series analysis is a well-  
 76 established technique for measuring ground deformation linked to interseismic strain ac-  
 77 cumulation (Fialko, 2006; Jolivet et al., 2013; Tong et al., 2013; Hussain, Hooper, et al.,  
 78 2016; Weiss et al., 2020), and has been shown in a couple of instances to be able to es-  
 79 timate interseismic fault slip rates down to a few millimeters per year (Bell et al., 2011;  
 80 Mousavi et al., 2015). The European Space Agency’s (ESA) Sentinel-1 C-band SAR satel-  
 81 lites provide previously unprecedented temporal coverage of data suitable for interfer-  
 82 ometry, with all of Iran being imaged on average every six days. Current sensing lim-  
 83 its for InSAR time series methods are 2–3 mm/yr for an average point velocity, given  
 84 a large number (hundreds) of acquisitions over a long time period (several years) and  
 85 in the presence of minimal noise (Morishita et al., 2020). The total time period covered  
 86 has a greater influence on the sensing threshold than the number of images used (Morishita  
 87 et al., 2020). Iran is generally a suitable target location for InSAR, given its relatively  
 88 arid climate and sparse vegetation cover. InSAR time series methods have been applied  
 89 to measure interseismic slip rates on a number of faults in the region, including the Ashk-  
 90 abad (5–12 mm/yr, Walters et al., 2013), Doruneh ( $2.5 \pm 0.3$  mm/yr Mousavi et al., 2021),  
 91 North Tabriz (6–10 mm/yr, Rizza et al., 2013; Karimzadeh et al., 2013; Su et al., 2016;  
 92 Aghajany et al., 2017), Shahroud ( $4.75 \pm 0.8$  mm/yr Mousavi et al., 2015), and the Minab-  
 93 Zendan-Palami (10 mm/yr) and Sabzevaran-Kahnuj-Jiroft (7.4 mm/yr) fault systems  
 94 (Peyret et al., 2009). However, InSAR has not previously been used to estimate the in-  
 95 terseismic motion across the MRF, despite the potential of this technique to better con-  
 96 strain both the slip rate and locking depth of this important fault.

97 Using ESA’s Sentinel-1 SAR satellites and 5.5 years of data covering a  $400 \times 200$  km  
 98 area centred on the MRF, we measure the relative horizontal motion in a velocity time  
 99 series to the millimeter per year level. We mitigate atmospheric noise contamination and  
 100 co- and post-seismic signals for the  $M_w$  7.3 Sarpol-e Zahab earthquake in 2017, and from  
 101 these corrected velocity data we investigate the fault kinematics of the MRF, namely the  
 102 rate of interseismic fault slip and the depth above which the fault is considered locked,  
 103 using a simple screw dislocation model (Savage & Burford, 1973) and following a Bayesian  
 104 framework to assess the uncertainties based upon the data noise. We conclude with a  
 105 discussion of the role of the MRF in accommodating convergence between the Arabian  
 106 and Eurasian plates, the extent of slip localisation, and the limitations of measuring tec-  
 107 tonic signals close to the current sensing limit of Sentinel-1 InSAR observations.

## 108 2 Tectonic Background

109 Iran constitutes one of the widest zones of continental convergence on a global scale  
 110 (Allen et al., 2004, 2013). Present day convergence rates between Arabia and Eurasia  
 111 are estimated at 15–25 mm/yr (McClusky et al., 2003; Khorrami et al., 2019) (Figure  
 112 1c). Convergence is roughly range-perpendicular in the southeastern Zagros, becoming  
 113 increasingly oblique up to  $45^\circ$  in the northwest. Talebian and Jackson (2004) first sug-  
 114 gested that deformation in the western Zagros is partitioned into range-perpendicular  
 115 shortening and range-parallel strike-slip motion, later supported by Iranian GNSS ve-

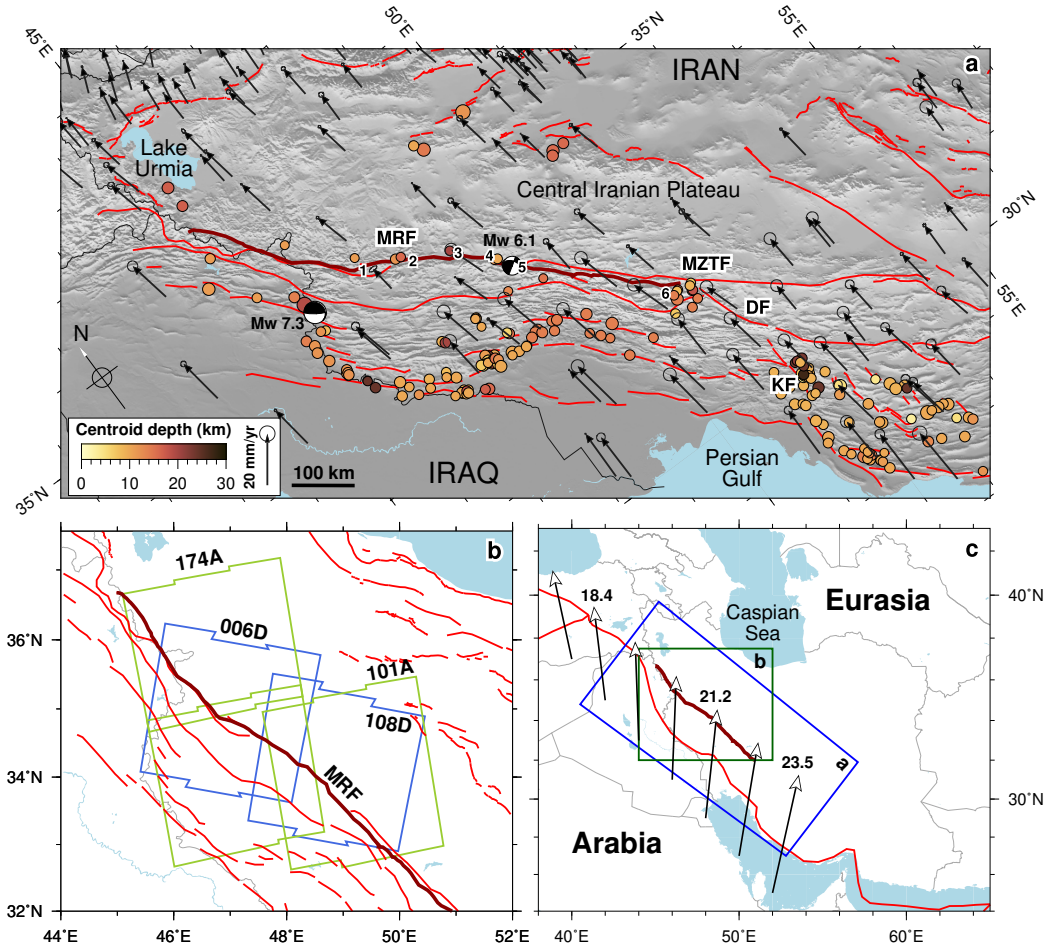


**Figure 1.** Overview of the study area in Western Iran. (a) Location of major faults (red lines) from Walker et al. (2010), with a 750 km section of the MRF highlighted in dark red. Vectors show GNSS velocities with  $1\sigma$  uncertainties from Khorrami et al. (2019) with respect to a stable Eurasia. Circles show relocated seismicity from Karasözen et al. (2019) covering 1962–2017, scaled by magnitude and coloured by centroid depth. MRF = Main Recent Fault, MZTF = Main Zagros Thrust Fault, DF = Dena Fault, KF = Kazerun Fault. Fault segments are numbered as: 1 - Kamyanan, 2 - Sahneh, 3 - Nahavand, 4 - Borujerd, 5 - Dorud, 6 - Ardal. (b) LiCS defined frames for Sentinel-1 InSAR coverage. A = Ascending orbital track, D = Descending orbital track. Focal mechanisms are shown for the  $M_w$  7.3 2017 Sarpol-e Zahab mainshock (Nissen et al., 2019) and the  $M_w$  6.1 2006 Silakhour mainshock (Ghods et al., 2012). (c) Plate boundary from Bird (2003) shown in red, Arabian plate velocities (mm/yr) relative to stable Eurasia (Kreemer et al., 2014).

**Table 1.** Previously published long-term geologic and geodetic interseismic slip rate estimates for the Main Recent Fault (top) and adjacent faults (bottom).

Study	Fault	Method	Rate (mm/yr)
Talebian and Jackson (2002)	MRF	Geological/geomorphological features	10–17
Bachmanov et al. (2004)	MRF : Dorud & Nahavand segments	Geological/geomorphological features	10
Vernant et al. (2004)	MRF	GNSS (regional)	3 ± 2
Copley and Jackson (2006)	MRF	Geological/geomorphological features	2–5
Walpersdorf et al. (2006)	MRF	GNSS (regional)	4–6
Authemayou et al. (2009)	MRF	Cosmogenic <sup>36</sup> Cl dating	3.5–12.5
Alipoor et al. (2012)	MRF	Geological, geomorphological markers, pullapart basins, and drainage patterns	1.6–3.2
Khorrani et al. (2019)	MRF	GNSS (regional)	2.7–4.0
Hessami et al. (2006)	Kazerun	GNSS (campaign profiles)	4–5
Walpersdorf et al. (2006)	Kazerun	GNSS (regional)	3 ± 2
	Dena		3 ± 2
Tavakoli et al. (2008)	Dena	GNSS	3.7 ± 0.8
	Kazerun		3.6 ± 0.6
Authemayou et al. (2009)	Kazerun (Northern strand)	Cosmogenic <sup>36</sup> Cl dating	2.5–4
	Kazerun (Central strand)		1.5–3.5

*Note.* Adjacent fault are provided for comparison and labelled in Figure 1. Studies are ordered by year of publication.

116 locity fields (Walpersdorf et al., 2006) and crustal stress maps (Zarifi et al., 2014). How-  
 117 ever, this partitioning may be incomplete (Vernant & Chery, 2006; Nissen et al., 2019).  
 118 At longitudes between 48°–55° E, 7–10 mm/yr of shortening is accommodated by range-  
 119 perpendicular movement on thrust faults (Vernant et al., 2004; Walpersdorf et al., 2006;  
 120 Khorrani et al., 2019). This decreases to 4–6 mm/yr moving westward to 42°–46° E.

121 The Zagros is also one of the most seismically active fold-and-thrust belts in the  
 122 world (Talebian & Jackson, 2004; Hatzfeld & Molnar, 2010; Nissen et al., 2011) (Figure  
 123 1a). Focal depths generally range between 4–25 km, nucleating in both the basement and  
 124 sedimentary cover in similar proportions, and with the majority failing to rupture to the  
 125 surface (Karasözen et al., 2019). Seismicity accounts for around half of the geodetic short-  
 126 ening rate in the northwestern Zagros, and less than a third in the southeast, implying  
 127 large amounts of folding, aseismic fault slip, and ductile shortening of the basement (Karasözen  
 128 et al., 2019). Rates of seismicity drop off rapidly northwest of the MRF in the Central  
 129 Iranian Plateau.

130 The Main Recent Fault trends NW-SE for over 800 km as a linear series of fault  
 131 segments (Figure 1). These segments may be characterised by their strike, which changes  
 132 from 330° northwest of Kamyanan, to 300° in the centre near Sahneh, and 315° south-  
 133 east of Borujerd (Talebian & Jackson, 2002). The overall slip vector is believed to be par-  
 134 allel to the central section (47–50° E), between 300° and 310°, suggesting oblique motion  
 135 on both northwestern and southeastern segments. The MRF cross-cuts the Main Zagros  
 136 Thrust Fault (MZTF), having partially inherited its fault trace west of 49° E (Tchalenko  
 137 & Braud, 1974). The MZTF traces the suture between the Arabian margin and the Iran-  
 138 ian block and is currently thought to be inactive (Walpersdorf et al., 2006). Relocated  
 139 seismic events also highlight slip on previously unmapped faults, suggesting continuing  
 140 evolution of the geometry of the MRF (Ghods et al., 2012). The MRF contains multi-  
 141 ple pull-apart basins (Talebian & Jackson, 2002; Authemayou et al., 2009; Sepahvand  
 142 et al., 2012), related either to the change in strike (Talebian & Jackson, 2002) or the chang-  
 143 ing convergence direction (Copley & Jackson, 2006). To the southeast, the MRF termi-  
 144 nates in a ‘horse tail’ structure formed by the Dena, Kazerun, Borazjan, Kareh Bas, and  
 145 Sarvestan faults (Bachmanov et al., 2004; Authemayou et al., 2009; Khorrani et al., 2019).  
 146 To the northwest, right-lateral motion continues into a complex dextral shear zone that  
 147 runs along the Arabian-Eurasian suture north of 37° N (Niassarifard et al., 2021). This  
 148 in turns joins two NNW-striking normal fault zones north of 37.5° N, which accommo-  
 149 date range-parallel motion through ESE-extension. Right-lateral strike-slip motion is re-

sumed on the North Tabriz fault in NW Iran (Aghajany et al., 2017) and the North Anatolian fault in Turkey (Hussain, Hooper, et al., 2016).

Calibrated earthquake relocations from Karasözen et al. (2019) show that the majority of earthquakes close to the MRF occur at depths shallower than 15 km. A minority of events are recorded at depths closer to 20 km, implying a likely locking depth of around 15–20 km. The 2006 Silakhour sequence, consisting of two foreshocks on the 30th March ( $M_b$  4.8 and 5.2) and a  $M_w$  6.1 mainshock on the 31st March, ruptured two patches of the MRF (Peyret et al., 2008; Ghods et al., 2012). These patches were on the western Nahavand-Borujerd and eastern Borujerd-Dorud segments, separated by 10 km of fault that did not rupture. The Nahavand-Borujerd patch was not associated with any known fault structure, suggesting ongoing development of the fault zone (Ghods et al., 2012). The largest historical earthquake believed to have occurred on the fault, a  $M_s$  7.4 earthquake near Dorud in 1909, ruptured 45–65 km of the fault (Ambraseys & Moinfar, 1973).

Large earthquakes have also occurred on adjacent faults, including the  $M_w$  7.3 Sarpol-e Zahab earthquake in 2017 (Barnhart et al., 2018; Nissen et al., 2019; K. Wang & Bürgmann, 2020) which ruptured a dextral-thrust fault beneath the Lurestan arc, 100–200 km south of the MRF. Ground surface deformation from the earthquake may be observable up to the MRF, which would constitute a source of error in our velocity estimates. The oblique slip direction highlights the incomplete partitioning of convergence onto reverse and strike-slip faults in the western Zagros. Similarly, the 2008 and 2012 Moosiyan earthquake sequences, which occurred on the Zagros foredeep fault, caused seismic and aseismic strike-slip motion on structures other than the MRF (Nippres et al., 2017). An accurate interseismic slip rate for the MRF will allow for an improved assessment of the degree of strain localisation and partitioning on the MRF. A measurable vertical velocity contrast across the MRF would suggest dip-slip motion and incomplete partitioning, as would a lower slip rate than needed to complete the plate-circuit-closure.

### 3 Methods

#### 3.1 InSAR Processing

We process a total of 1038 Sentinel-1 Interferometric Wide Swath images across two ascending tracks (174 and 101) and two descending tracks (006 and 108), with an average time span of 5.6 years from late 2014 to mid 2020 (Table 2). From these images, we produce a total of 4634 interferograms. Interferograms are formed between each acquisition and the three previous epochs to form a redundant network with minimised temporal baselines (Figure S1). Additionally, we produced long temporal baseline interferograms to bridge periods of low coherence (e.g. winter). We manually remove a total of 52 interferograms due to unresolved processing errors.

We generate interferograms using the LiCSAR system, a set of high-level tools and algorithms that operate the GAMMA SAR and Interferometry software (Werner et al., 2000; Wegmüller et al., 2016). The reader is referred to Lazecky et al. (2020) for an in-depth description of the processing system. Images are processed in predefined frames that average 13 bursts across each of the three subswaths that were acquired in Terrain Observation with Progressive Scans (TOPS) mode. We remove topographic contributions to the phase return using the 1 arc-second SRTM DEM (Farr et al., 2007). We unwrap each interferogram in two dimensions using the statistical-cost network-flow algorithm (SNAPHU) version 2 (Chen & Zebker, 2000, 2001, 2002). Interferograms are multilooked by 20 in range and 4 in azimuth (46.6×55.9 m) during the processing, and then further downsampled to 100 × 100 m pixels outside of GAMMA.

Atmospheric noise is often the largest source of error in InSAR data and results from spatially-correlated radar path delays as waves are refracted through the troposphere

**Table 2.** Time extent and number of processed SAR data for each track used in this study.

Track	Start	End	Duration (yr)	no. of epochs	no. of ifgs generated	no. of ifgs used	mean ifg length (d)
006D	2014-10-06	2020-07-06	5.75	196	1022	997	10.8
108D	2014-10-25	2020-07-13	5.72	204	1024	987	10.3
174A-N	2014-11-10	2020-06-23	5.62	219	984	939	9.5
174A-S	2014-11-10	2020-06-23	5.62	206	884	878	10.0
101A	2015-02-09	2020-07-06	5.41	213	720	665	9.3

*Note.* A = ascending orbital tracks (acquisition time 14:43-14:52 UTC, 18:13-18:22 IRST, 19:13-19:22 IRDT), D = descending orbital tracks (acquisition time 02:45-02:52 UTC, 06:15-06:22 IRST, 07:15-07:22 IRDT). Typically about 200 SAR images are used to produce 700-1000 interferograms (ifgs) (no. of ifgs generated) spanning a 6 to 12 day period (10 days on average), which are then reduced in number by various quality checks (no. of ifgs used). 174A-N and 174A-S refer to the northern and southern frames shown in Figure 1b, respectively.

UTC = Coordinated Universal Time, IRST = Iranian Standard Time, IRDT = Iranian Daylight Time

200 (Zebker et al., 1997; Parker et al., 2015). We mitigate this error using the Generic At-  
 201 mospheric Correction Online Service for InSAR (GACOS) (Yu et al., 2017; Yu, Li, & Penna,  
 202 2018, 2018), which provides tropospheric delay maps derived from the European Cen-  
 203 tre for Medium-Range Weather Forecasts (ECMWF) upscaled through use of a DEM.  
 204 These maps include both hydrostatic and wet components. ECMWF models are pro-  
 205 vided every six hours and can be interpolated to any SAR acquisition time in between.  
 206 For each interferogram, the respective tropospheric zenith delay maps are differenced,  
 207 projected into the satellite line-of-sight (LOS), and then subtracted from the interfer-  
 208 ogram. Figure 2 shows the change in the standard deviation of each interferogram af-  
 209 ter the GACOS correction has been applied. On average, 81% of interferograms for each  
 210 frame show a decrease in the standard deviation, associated with a reduction in atmo-  
 211 spheric noise, following the application of the GACOS correction, assuming that no tec-  
 212 tonic signal is visible in the short time span interferograms.

213 Next, we use LiCSBAS, a small-baseline time-series analysis package, to generate  
 214 cumulative line-of-sight displacements and average velocities from our interferograms (Morishita  
 215 et al., 2020; Morishita, 2021). We further downsample our 100×100 m interferograms  
 216 to 1 km to reduce processing requirements while retaining sufficient resolution to cap-  
 217 ture short-wavelength tectonic signals. Interferograms with low average coherence (< 0.05)  
 218 and low coverage (< 0.3) are identified and removed. We identify phase unwrapping er-  
 219 rors by calculating the loop closure phase,  $\Phi$  of every interconnected image triplet fol-  
 220 lowing Equation 1 (Biggs et al., 2007):

$$221 \quad \Phi_{123} = \phi_{12} + \phi_{23} - \phi_{13} \quad (1)$$

222 where  $\phi_{12}$ ,  $\phi_{23}$ , and  $\phi_{13}$  are the interferograms formed from SAR images  $\phi_1$ ,  $\phi_2$ , and  $\phi_3$ .  
 223 Near-zero values of  $\Phi$  for a triplet indicate that the unwrapping is consistent between  
 224 all three interferograms, while values near integer multiples of  $2\pi$  indicate the presence  
 225 of unwrapping errors in at least one interferogram. We calculate the root mean square  
 226 (RMS) of the loop phase image for every triplet and remove a total of 116 interferograms  
 227 where the RMS is greater than 1.5 rad for every loop that the interferogram is a part  
 228 of. Cumulative LOS displacements are inverted for a linear velocity on a pixel-by-pixel  
 229 basis following the NSBAS least-squares method (Doin et al., 2011), using the 4466 in-

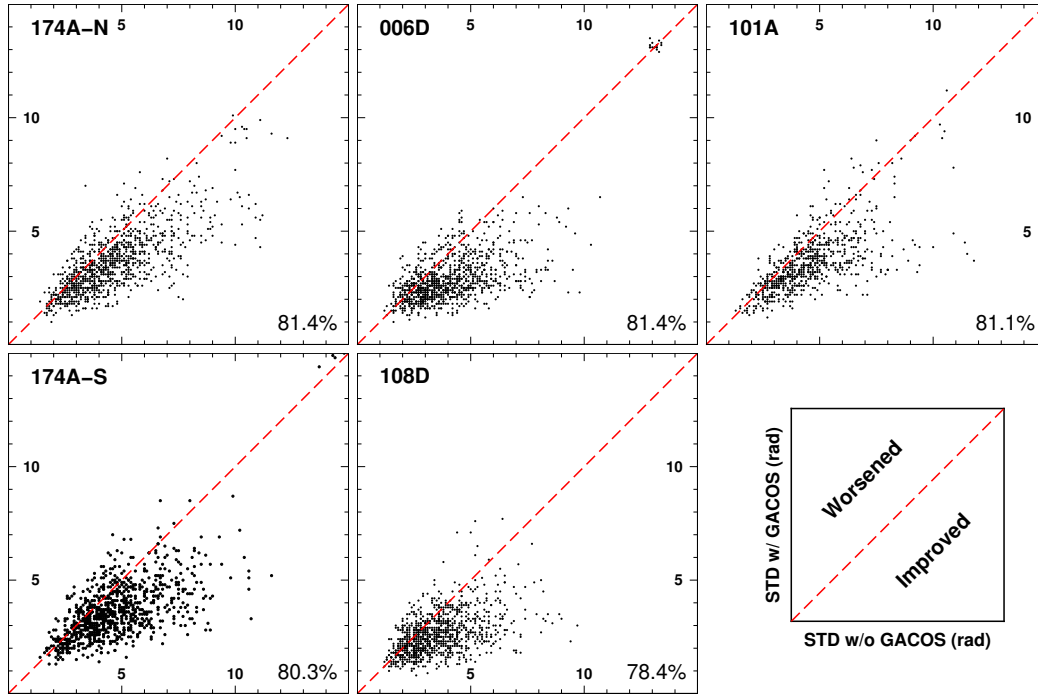


**Figure 2.** Change in the standard deviation (SD) of all pixels in each interferogram resulting from the application of the GACOS correction, with black dots below the red dashed line indicating an improvement in terms of interferogram noise from the application of the atmospheric model. The percentage of interferograms showing a reduction in SD for each frame is given in the bottom right of each subpanel. The distinct high SD clusters seen in 006D and 174A-S are associated with the  $M_w$  7.3 earthquake.

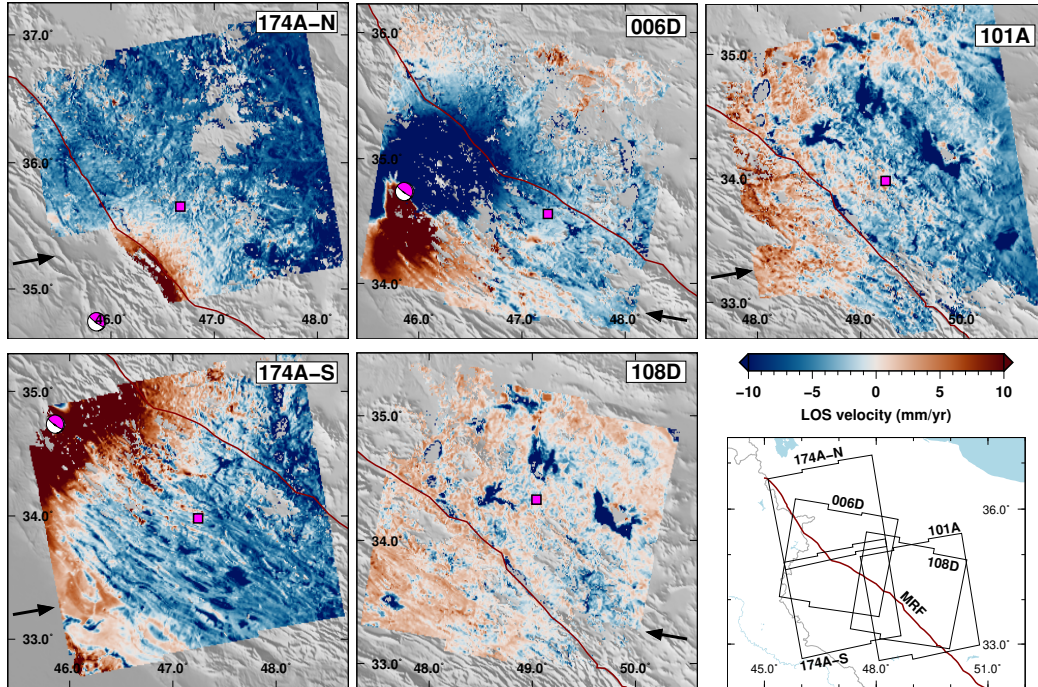


**Figure 3.** Average line-of-sight velocities for ascending and descending tracks at 1 km resolution. Black arrows show the horizontal projection of LOS vector. Red and blue indicate motion towards and away from the satellite, respectively, relative to a reference pixel (pink squares). The effect of the  $M_w$  7.3 2017 Sarpol-e Zahab mainshock (pink focal mechanism) is clearly visible in frames 174A-N, 174A-S and 006D as the large positive and negative velocity areas saturated in this image. A number of subsiding basins are visible as regions with rates faster than -10 mm/yr.

230 interferograms that passed the quality checks. In the case of missing observations in the  
 231 displacement time series (e.g. incoherence, missing acquisitions, masked pixels), LiCS-  
 232 BAS imposes a linear temporal constraint across the gap. These estimated displacements  
 233 may be unreliable if the displacement series deviates significantly from a linear function.  
 234 Therefore, we avoid network gaps where possible by generating additional interferograms.  
 235 The average velocities are referenced to a stable pixel in each frame, chosen by calcu-  
 236 lating the RMS of all the loop closure phases for each pixel and selecting the lowest, with  
 237 the requirement that the pixel must be unmasked in every interferogram. We estimate  
 238 the uncertainty on the velocities by applying the percentile bootstrap method (Efron &  
 239 Tibshirani, 1986) to the cumulative displacements for each pixel. Each displacement series  
 240 is randomly resampled with data replacement 100 times and the velocity is re-calculated.  
 241 The standard deviation of the final 100 velocities is taken as the uncertainty on the LOS  
 242 velocity. A number of statistical quality checks are used to threshold a mask for the ve-  
 243 locity map (Figures S2–S6). The LOS velocity maps for each frame are shown in Fig-  
 244 ure 3. Example displacement series for two pixels, one across-fault difference and one sub-  
 245 sidence signal, are shown in Figures S7 and S8.

### 246 3.2 Evaluation of Co- and Post-seismic Signals

247 Tracks 174A and 006D span (both spatially and temporally) the 12 November 2017  
 248  $M_w$  7.3 Sarpol-e Zahab earthquake (Nissen et al., 2019) and subsequent aftershock se-  
 249 quences (Lv et al., 2020). The earthquake involved dextral-thrust slip on a  $40 \times 20$  km  
 250 basement fault in the Lurestan arc, potentially triggering aftershocks up to 80 km away.

251 Displacements of up to 90 cm in LOS were observed in Sentinel-1 interferograms span-  
 252 ning the event (Nissen et al., 2019). The first main aftershock sequence occurred on 11  
 253 January 2018, consisting of five events between  $M_w$  5.1–5.5 (Lv et al., 2020). The sec-  
 254 ond occurred on 25 November 2018 and consisted of  $M_w$  6.3, 5.2, and 5.0 events. In the  
 255 one year period following the mainshock, an additional 100 mm of LOS displacement was  
 256 observed related to postseismic deformation (K. Wang & Bürgmann, 2020). For areas  
 257 affected by the Sarpol-e Zahab earthquake, any estimate of the interseismic slip rate will  
 258 be biased by the co- and post-seismic displacements (Figure 3). A full assessment of the  
 259 magnitude and spatial extent of these signals in the InSAR velocity field is required so  
 260 as to be able to robustly estimate the interseismic slip rate.

261 We first attempt to mitigate the coseismic signals by forwarding modelling the dis-  
 262 placements and subtracting these from the cumulative displacements generated by LiCS-  
 263 BAS. For the mainshock, we use fault parameters estimated by Nissen et al. (2019) from  
 264 Sentinel-1 interferograms and a uniform slip fault model (Table S1). We model both aft-  
 265ershock sequences as a single event using InSAR-derived fault parameters from Lv et  
 266 al. (2020). The fault is modelled using a rectangular dislocation source (Okada, 1985)  
 267 defined by nine parameters: x-position, y-position, strike, dip, rake, slip, fault length,  
 268 top depth, and bottom depth. We chose InSAR-derived fault parameters, as opposed to  
 269 those from seismology, as they may more accurately fit our own observed InSAR signals.  
 270 Modelled surface displacements are projected into the satellite LOS for each frame and  
 271 then removed from the cumulative displacement series.

272 Next, we calculate the change in the average LOS velocity following the 12 Novem-  
 273 ber 2017  $M_w$  7.3 mainshock. To do this, we split the cumulative displacement time se-  
 274 ries produced by LiCSBAS into two parts about 12 November 2017 and solve for the av-  
 275 erage velocity pre- and post-earthquake using least squares. We do not attempt to re-  
 276 move the post-seismic signal from the times series (K. Wang & Bürgmann, 2020), as the  
 277 signal is difficult to separate from the noise and any errors could be of a similar mag-  
 278 nitude to the interseismic signal. Pixels for which the average velocity changed signif-  
 279 icantly following the earthquake may have been affected by post-seismic deformation.  
 280 The reduction in time series length to 2-3 years either side of the earthquake will increase  
 281 the velocity uncertainties to 4-5 mm/yr (Morishita et al., 2020). Additionally, the time  
 282 series before the earthquake contain fewer interferograms because Sentinel-1B was in-  
 283 active for some of this time period (2014–2017). We calculate the velocity difference for  
 284 the three affected frames and combine them by averaging overlapping pixels. We esti-  
 285 mate the expected velocity difference as a result of noise and non-tectonic signals by cal-  
 286 culating the velocity difference for 108D, which should be unaffected by the Sarpol-e Za-  
 287 hab earthquake sequence. We calculate a standard deviation of 11.4 mm/yr, and con-  
 288 tour the merged velocity differences based on the 95% confidence interval. Figure 4 shows  
 289 the merged and contoured velocity differences for frames 006D, 174A-N, and 174A-S. The  
 290 primary post-seismic signal is highlighted by the pink square and covers an area of ap-  
 291 proximately  $100 \times 150$  km. We observe a similar spatial extent to the cumulative post-  
 292 seismic displacements observed by K. Wang and Bürgmann (2020, Figure 4). The true  
 293 extent of the post-seismic deformation likely extends further than the highlighted area,  
 294 given the uncertainty in our velocities and the threshold used, and so we avoid veloci-  
 295 ties west of  $47^\circ$  E when selecting profile lines.

### 296 3.3 Velocity Field Generation

297 Our initial LOS InSAR velocity fields are referenced relative to a stable pixel for  
 298 each frame (pink squares in Figure 3). To better combine all four tracks, we shift the  
 299 LOS velocities into a Eurasia-fixed reference frame (Hussain, Hooper, et al., 2016; Hus-  
 300 sain et al., 2018; Weiss et al., 2020). Using horizontal GNSS velocities provided by Khorrami  
 301 et al. (2019), we fit second-order polynomial surfaces to the East and North velocity com-  
 302 ponents within one degree of our study area (Figure 5). The velocities are weighted us-

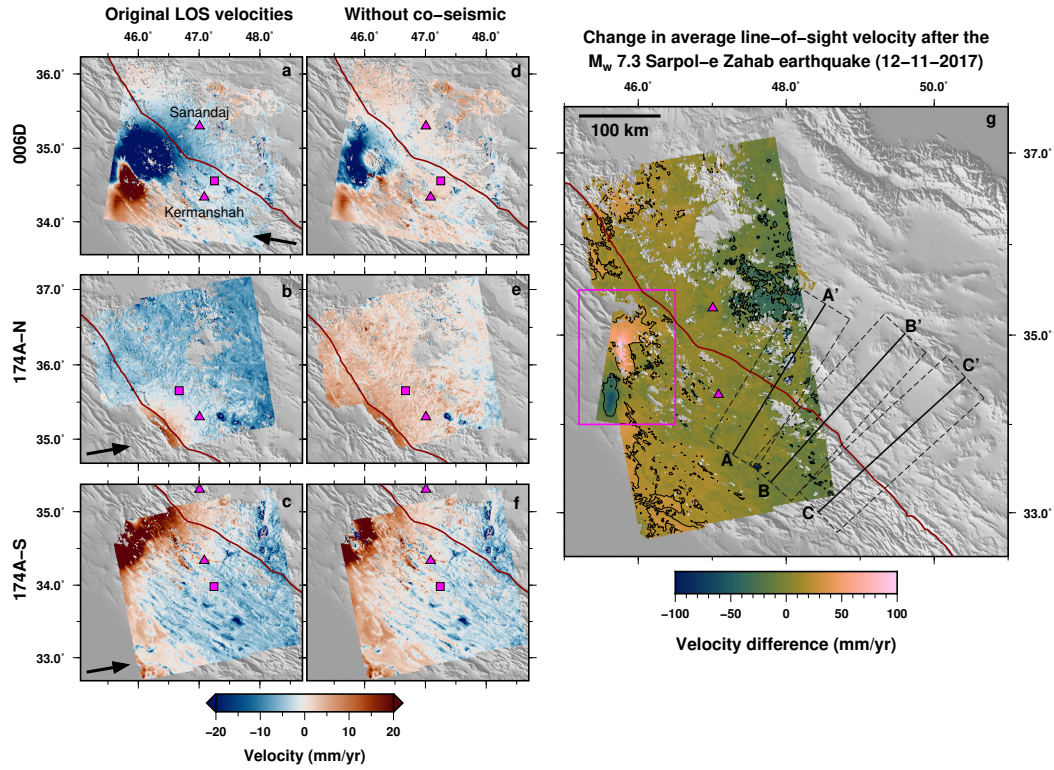


**Figure 4.** Analysis of co- and post-seismic signals following the  $M_w$  7.3 2017 Sarpol-e Zahab earthquake sequence. (a-c) Original line-of-sight velocities for frames 006D, 174A-N, and 174A-S, relative to the reference pixel (pink square). Two cities, Sanandaj and Kermanshah, are marked as pink triangles for spatial reference, along with the trace of the MRF (red). Black arrows show the horizontal projection of the LOS vector. (d-f) LOS velocities after the forward models for the earthquakes shown in Table S1 have been removed from the displacement time series, relative to the reference pixel (pink square). (g) Difference in average line-of-sight velocities before and after the 12 November 2017  $M_w$  7.3 mainshock, for frames 006D, 174A-N, and 174A-S. For overlapping pixels between frames, the values have been averaged. The values are contoured at  $\pm 23$  mm/yr, based upon the  $2\sigma$  value derived from frame 108D which is unaffected by the earthquake deformation. The pink rectangle highlights the region encompassing the main post-seismic signal. We choose profiles (A-A', B-B', and C-C') that avoid areas with significant velocity changes following the earthquake.

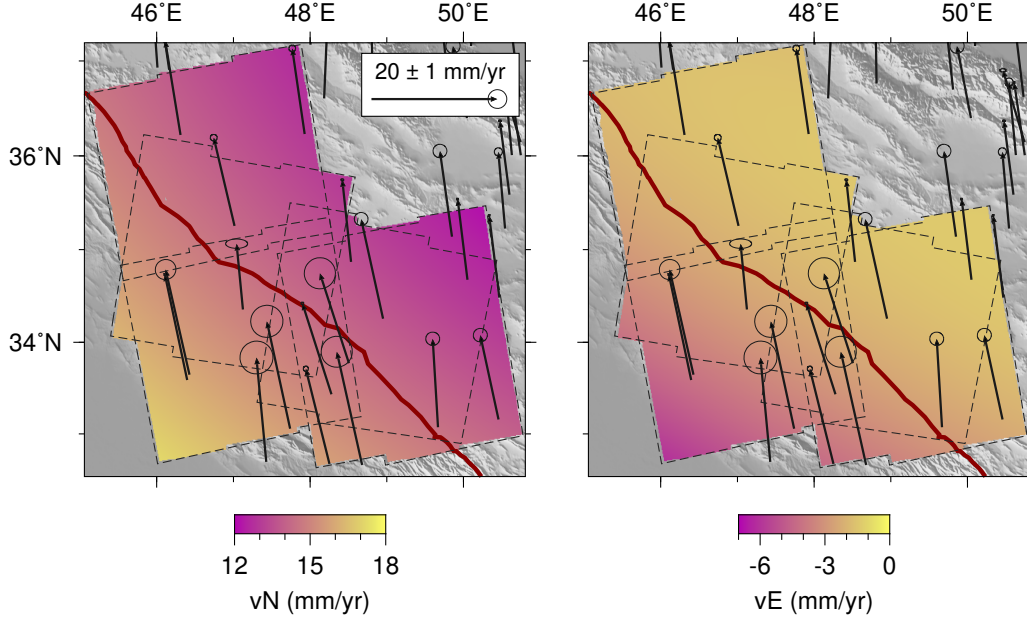


**Figure 5.** Spatially interpolated GNSS velocity fields generated by fitting a 2nd-order polynomial plane to North ( $v_N$ ) and East ( $v_E$ ) GNSS velocities from Khorrami et al. (2019) relative to a stable Eurasia, cropped to the area covered by the InSAR. GNSS velocities are located at the base of the arrows and given with  $1\sigma$  uncertainties.

303 ing their respective bootstrapped uncertainties. We then project the GNSS velocity fields  
 304 are projected into the satellite LOS for each frame. We calculate the residual between  
 305 the projected GNSS velocities and the InSAR velocities, and fit a second-order poly-  
 306 nomial surface to the result. Subtracting this function from the respective InSAR veloci-  
 307 ty field results in InSAR velocities in the same reference frame as the GNSS velocities.

308 To investigate interseismic slip along the MRF, we decompose our satellite LOS  
 309 velocities into local geodetic coordinate velocities. The velocity for each pixel observed  
 310 in the satellite LOS can be expressed as a linear combination of the East, North, and  
 311 Up components:

$$312 \quad V_{LOS} = \begin{bmatrix} \sin(\theta)\cos(\alpha) & -\sin(\theta)\sin(\alpha) & -\cos(\theta) \end{bmatrix} \begin{bmatrix} V_E \\ V_N \\ V_U \end{bmatrix} \quad (2)$$

313 where  $\theta$  is the radar incidence angle, measured from the vertical to the LOS, and  $\alpha$  is  
 314 the azimuth of the along-track satellite heading. The majority of our study area is cov-  
 315 ered by two overlapping tracks, one ascending and one descending. In this situation, we  
 316 have two observations ( $V_{asc}$  and  $V_{desc}$ ) and three unknowns ( $V_E$ ,  $V_N$ , and  $V_U$ ), making  
 317 the inverse problem under-determined. In order to find a unique solution to the prob-  
 318 lem, we must add either further observations or a-priori constraints for one of the model  
 319 parameters. Sentinel-1 InSAR observations are particularly insensitive to displacement  
 320 in the north-south direction, as a result of the near-polar satellite orbit and sideways  
 321 look direction. We estimate the north contribution to the InSAR LOS velocities by pro-  
 322 jecting the interpolated north GNSS velocity field (Figure 5) into the respective satel-  
 323 lite LOS for each track. This projected velocity is then subtracted from each frame, leav-  
 324 ing LOS velocities that contain a negligible long-wavelength north-south component. For  
 325 a point with observations from two look directions, the resulting simplified linear equa-

326 tion is given by Equation 3.

$$327 \begin{bmatrix} V_{asc} \\ V_{desc} \end{bmatrix} = \begin{bmatrix} -\cos(\theta_{asc}) & \sin(\theta_{asc})\cos(\alpha_{asc}) \\ -\cos(\theta_{desc}) & \sin(\theta_{desc})\cos(\alpha_{desc}) \end{bmatrix} \begin{bmatrix} V_U \\ V_E \end{bmatrix} \quad (3)$$

328 In the presence of three or more overlapping frames, the 2-by-2 matrix in Equation 3 can  
 329 be expanded to a  $n$ -by-2 matrix, where  $n$  is the number of overlapping frames. We solve  
 330 Equation 3 using weighted least squares and the data variance-covariance matrix (VCM).  
 331 The data VCM is a  $n$ -by- $n$  matrix containing the bootstrapped variance values gener-  
 332 ated by LiCSBAS for a given point, and assuming no covariance between the same point  
 333 in different frames. We also calculate the model VCM following Equation 4:

$$334 Q_m = (G'WG)^{-1} \quad (4)$$

335 where  $Q_m$  is the 2-by-2 model VCM,  $G$  is the design matrix (the  $n$ -by-2 matrix in Equa-  
 336 tion 3), and  $W$  is the inverse of the data VCM. Uncertainties for the decomposed veloc-  
 337 ities (Figure S9) are typically in the range of 0.2–1.0 mm/yr in the East component and  
 338 0.5–1.5 mm/yr in the Up component.

### 339 3.4 Interseismic Fault Slip Modelling

340 We model profiles of the InSAR-derived velocities across the deforming zone by as-  
 341 suming that the fault can be approximated as a vertical buried 1-D screw dislocation (Savage  
 342 & Burford, 1973) defined by Equation 5:

$$343 v_{para}(x) = \left(\frac{s}{\pi}\right) \arctan\left(\frac{x}{d}\right) + c \quad (5)$$

344 where  $v_{para}(x)$  is the horizontal surface velocity parallel to the fault,  $x$  is the perpen-  
 345 dicular distance from the fault,  $s$  is the interseismic slip rate,  $d$  is the locking depth, and  
 346  $c$  is a scalar offset. We calculate fault-parallel velocities using the decomposed east In-  
 347 SAR velocities and the north component of the GNSS velocity field, using the local strike  
 348 within each profile. We take three 70 km wide fault-perpendicular profiles across the MRF  
 349 (A-A', B-B', and C-C'), avoiding areas with post-seismic signals (Figure 4). We solve  
 350 for the interseismic slip rate, the locking depth, and a scalar offset to the velocities (Equa-  
 351 tion 5), assuming strikes of 300°, 310°, and 315° for A-A', B-B', and C-C', respectively.  
 352 We fix the fault location based upon the intersection of the profile lines with the fault  
 353 trace from Walker et al. (2010), and apply a scalar offset to the velocities so that the pro-  
 354 files are centred on approximately 0 mm/yr where they intersect the fault trace.

355 We estimate best fit values for each model parameter by implementing an affine-  
 356 invariant ensemble Markov Chain Monte Carlo (MCMC) sampler, developed by Goodman  
 357 and Weare (2010). This Bayesian approach uses semi-random walks of a given number  
 358 of walkers to explore the posterior probability distribution of the model, based upon known  
 359 prior constraints. Solutions are ranked using the weighted misfit between observed and  
 360 model velocities. It demonstrates improved performance over traditional Metropolis-Hasting  
 361 algorithms, especially in the presence of complex parameter spaces (Goodman & Weare,  
 362 2010). This method has been widely used for tectonic applications (Hussain, Wright, et  
 363 al., 2016; Hussain, Hooper, et al., 2016; Szeliga & Bilham, 2017; Aslan et al., 2019; Goto  
 364 et al., 2019; Tesson et al., 2021). Our MCMC sampler uses 600 walkers and runs for 300,000  
 365 iterations. We remove the first 20% of solutions as burn-in, producing 48,000 valid so-  
 366 lutions. From these we calculate the maximum a posteriori probability (MAP) solution  
 367 - i.e. the most likely solution based upon the prior probabilities - and uncertainties for  
 368 each model parameter. We assume a uniform prior for all model parameters based upon  
 369 limits of  $-10 \leq s \leq 20$  (mm/yr),  $1 \leq d \leq 50$  (km), and  $-10 \leq c \leq 10$  (mm/yr).

370 To account in the inversion for the noise of the data and correlation between nearby  
 371 pixels, we calculate the spatial covariance function of the data after removing tectonic  
 372 and anthropogenic signals (e.g. Hussain, Hooper, et al., 2016; Weiss et al., 2020). We

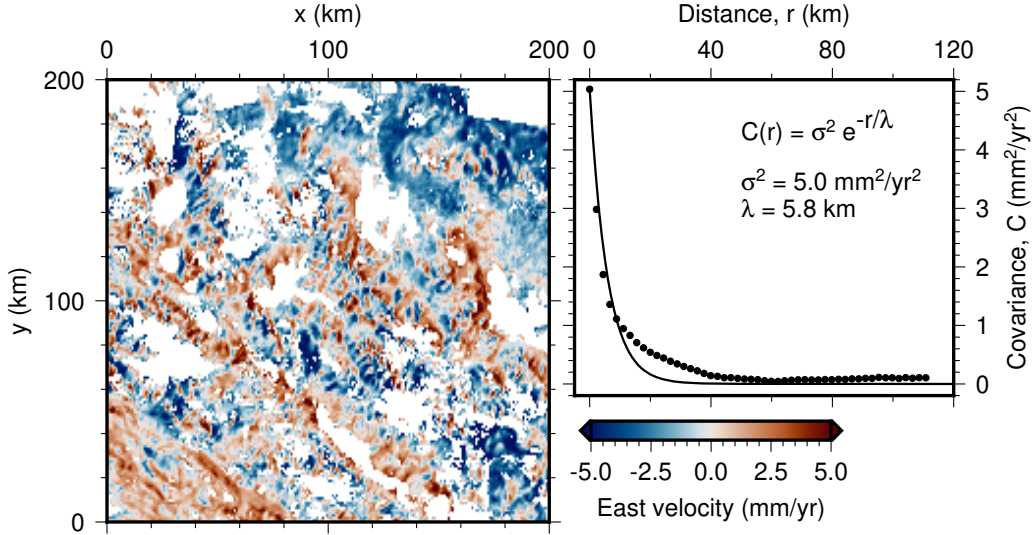


**Figure 6.** Autocorrelation function and best-fitting exponential (Equation 6) (right) based upon isolated non-tectonic and non-anthropogenic noise in the East InSAR average velocities (left).

373 take a  $200 \times 200$  km region of the decomposed East velocities, avoiding the post-seismic  
 374 signals in the west of the study area, and mask out any pixels associated with a verti-  
 375 cal rate greater than  $\pm 5$  mm/yr; these signals are largely correlated with basins and are  
 376 likely due to groundwater subsidence. We forward model the interseismic slip on the MRF  
 377 using Equation 5, assuming a slip rate of 3 mm/yr below a locking depth of 20 km, and  
 378 subtract the East component of this model from our decomposed east velocities. Finally,  
 379 we remove a first-order polynomial plane from the velocities to account for any resid-  
 380 ual tectonic signal or orbital ramps. The resulting velocities (Figure 6) should contain  
 381 negligible tectonic and anthropogenic signals, with the majority of the velocity field con-  
 382 sisting of short-wavelength residual atmospheric noise that remained after the GACOS  
 383 correction (Murray et al., 2019). We fit an exponential radial covariance function (Hussain,  
 384 Hooper, et al., 2016) to these data of the form:

$$385 \quad C(r) = \sigma^2 e^{-\frac{r}{\lambda}} \quad (6)$$

386 where  $C(r)$  is the covariance between two velocity measurements at a distance of  $r$ ,  $\sigma^2$   
 387 is the variance, and  $\lambda$  is the exponential length scale. We solve Equation 6 for  $\sigma^2$  and  
 388  $\lambda$ , estimating values of  $5.0 \text{ mm}^2/\text{yr}^2$  and 5.8 km, respectively (Figure 6). The misfit be-  
 389 tween  $r$  values of 10–40 km, where the covariance model underestimates the observed  
 390 decay in noise at mid distances, relates to asymmetry within the noise structure. This  
 391 is potentially as a result of NW-SE aligned topographic structures (mountain ranges and  
 392 interleaved valleys) with similar widths and lengths. We generate a variance-covariance  
 393 matrix for all pixels within each profile using Equation 6 and our estimated exponen-  
 394 tial parameters, where  $r$  is the 2-D distance between pixels, and use this to weight our  
 395 Bayesian inversion.

## 396 4 Results

397 Figure 7 shows the decomposed East, vertical, and fault-parallel velocities, the lat-  
 398 ter of which was calculated assuming a fixed strike of  $310^\circ$ . We observe higher veloci-  
 399 ties (red) to the northeast in both the East and fault-parallel velocities, with a veloc-

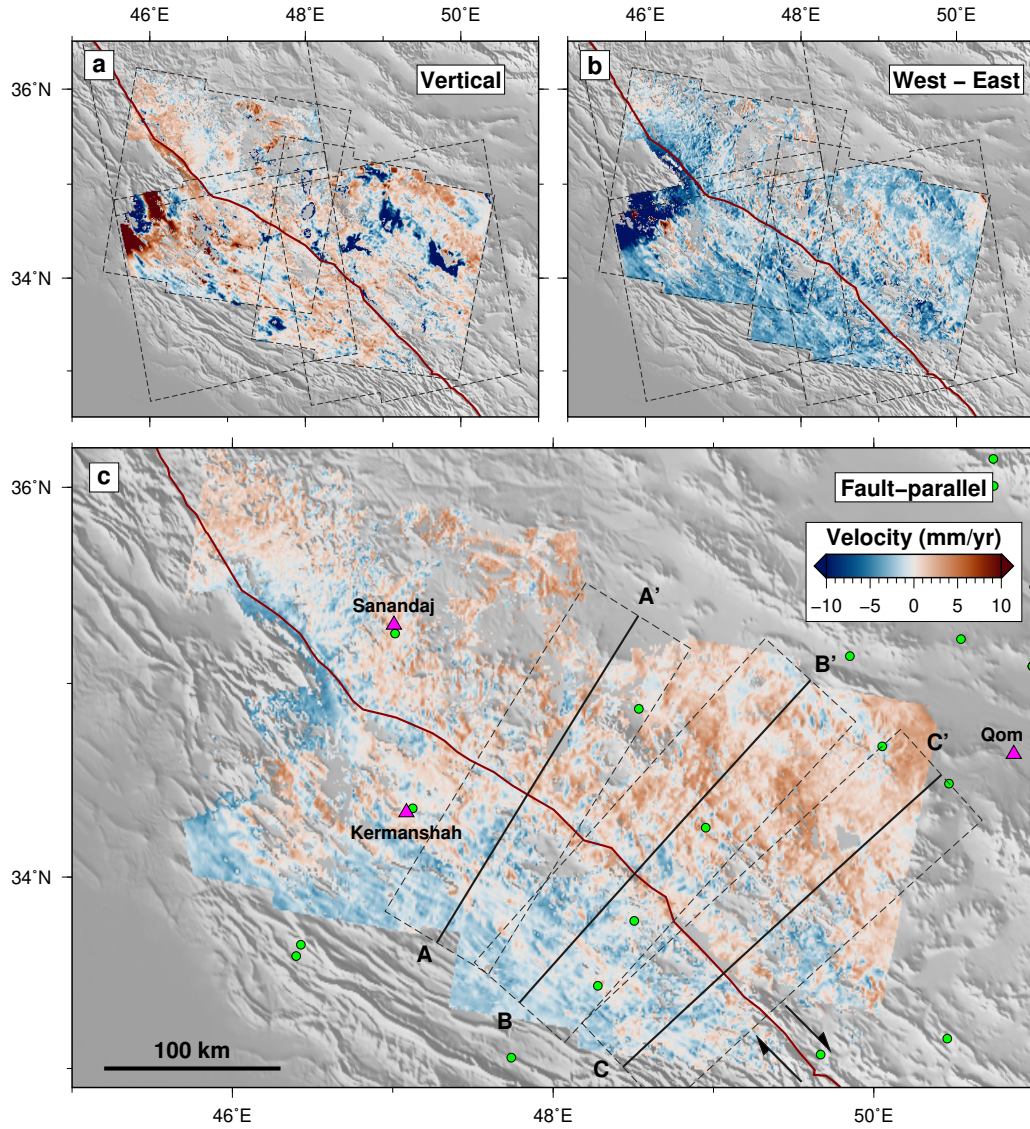


**Figure 7.** Decomposed Vertical (a) and East (b) velocities, and fault-parallel (c) velocities assuming an overall regional fault strike of  $310^\circ$ , relative to the MRF. Positive values (red) indicate motion upwards, to the east, and in a right-lateral sense, respectively. Fault-perpendicular profiles (black lines) are taken perpendicular to the projected MRF trace (red line). Velocities are overlain onto hill-shaded SRTM topography, with city locations (pink triangles) and GNSS locations (green circles) marked for reference.

**Table 3.** Maximum a posteriori probability estimates and uncertainties of the parameters in Equation 5 for the three profiles shown in Figure 7, for both independent (Ind) profiles and the three-profile joint model with a shared locking depth.

		A-A'		B-B'		C-C'	
Ind	$s$ (mm/yr)	2.6	(1.2–4.6)	2.9	(1.6–4.7)	3.5	(1.0–4.7)
	$d$ (km) (95% IQR)	18.4	(5.6–48.9)	19.4	(7.1–48.6)	49.7	(unbounded)
	$c$ (mm/yr)	-0.0	(-0.5–0.4)	0.2	(-0.3–0.6)	-0.8	(-1.2– -0.2)
Joint	$s$ (mm/yr)	2.8	(1.2–4.8)	3.1	(1.5–4.7)	2.6	(1.1–4.7)
	$d$ (km)			29.0	(18.7–41.9)		
	$c$ (mm/yr)	-0.1	(-0.8–0.8)	-0.2	(-0.6–0.9)	-0.7	(-1.4–0.3)

*Note.* Results are given with 95% confidence intervals with the exception of the locking depths for the individual A-A' and B-B' results, which are given with 95% interquartile ranges (IQR), as these distributions are significantly non-Gaussian (Figures 9).

ity difference across the MRF of several millimeters per year. The velocity difference is lower west of 47.5° E where we expect the velocities to be biased by the Sarpol-e Zahab earthquake sequence (Figure 4). No equivalent velocity contrast can be seen in the vertical velocities. The large negative (blue) velocities previously observed in the LOS velocities are now only present in the vertical velocities, supporting the idea that these are subsidence signals related to groundwater extraction.

Figure 8 shows the results of the MCMC inversion, and Figure 9 shows the marginal posterior probability distributions for each parameter. MAP solutions and uncertainties for each parameter are given in Table 3. We include the mean and standard deviation of the fault-parallel velocities (Figures 8 and 10), weighted using the variance of the East velocities (Figure S6) and calculated in a 10 km window moved in 1 km increments along the profiles.

Our MAP estimates of slip rate are consistent between profiles A-A' (2.6 mm/yr), B-B' (2.9 mm/yr), and C-C' (3.5 mm/yr), to within the 95% confidence intervals (1.2–4.6, 1.6–4.7, and 1.0–4.7 mm/yr, respectively) (Table 3). We see similar consistency between our MAP estimates of locking depth for profiles A-A' (18.4 km) and B-B' (19.4 km). The posterior distributions for both are either skewed (B-B') or non-Gaussian (A-A'), and so we provide the 95% interquartile range (IQR), defined as the difference between the 0.025 and 0.975 quantiles, for A-A' (5.6–48.9 km) and B-B' (7.1–48.6 km) as this is more representative. The upper locking depth for B-B' may also be considered unbounded, given that the distribution levels off above 20 km. Profile C-C' may be considered unbounded within the parameter range we have chosen, tending towards a very deep locking depth.

To better constrain the locking depth, we subsequently model the velocities across all three profiles simultaneously. We estimate a shared locking depth across all three profiles and keep separate solutions of profile-specific slip rates and offsets, otherwise repeating the previous setup. We would expect the locking depth to be approximately constant across relatively short section of a major fault. Figure 10 shows the results of the MCMC inversion, Figure 11 shows the marginal posterior probability distributions for each parameter, and Table 3 summarises the MAP estimates and uncertainties. Our MAP estimates of slip rate are again consistent across profiles A-A' (2.8 mm/yr), B-B' (3.1 mm/yr), and C-C' (2.6 mm/yr) to within the 95% confidence intervals (1.2–4.8 mm/yr, 1.5–4.7 mm/yr, and 1.1–4.7 mm/yr, respectively). The posterior distribution for our joint estimate of

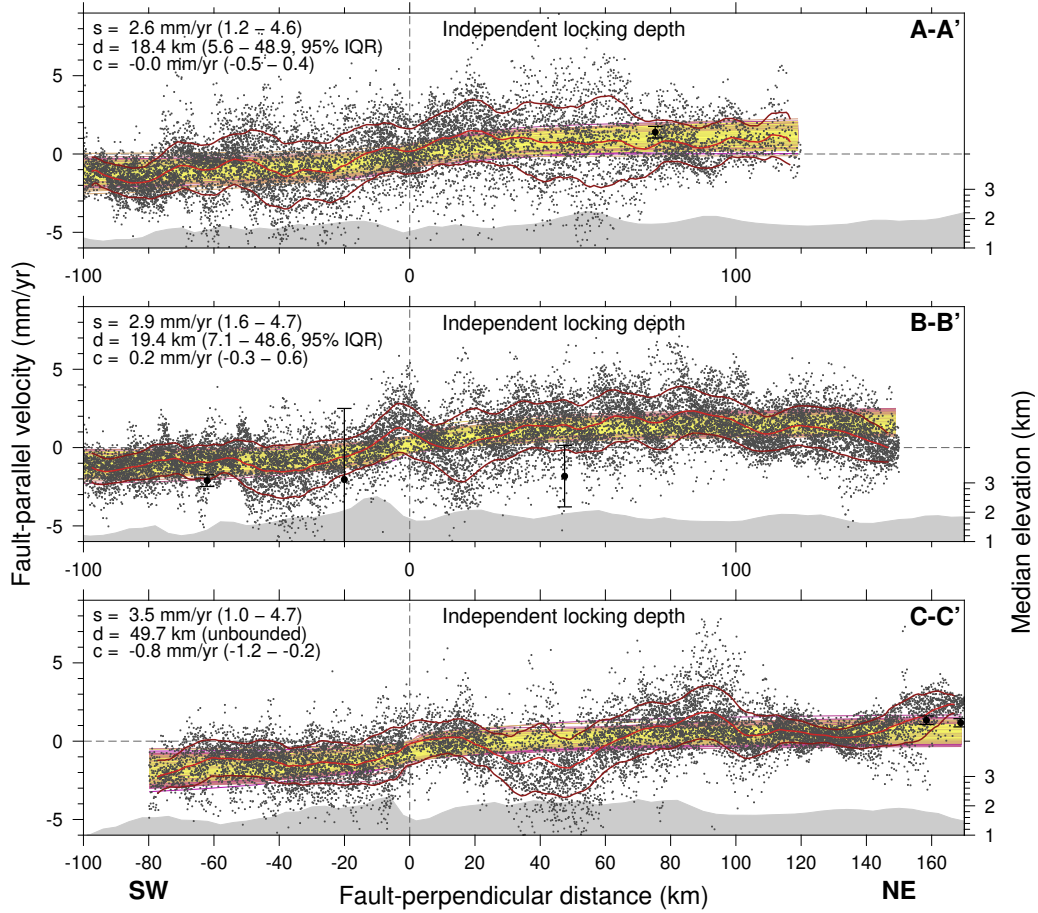


**Figure 8.** Northeast-southwest profiles of fault-parallel (strike direction) velocity (with positive motion to the SE shown by the black dots) relative to the surface trace of the MRF (set at zero distance), from Figure 7, modelled with independent locking depths. The light and dark red lines show the weighted average and weighted standard deviation of the velocities, respectively. A uniformly randomly selected 1% of modelled solutions are shown ranked by the posteriori probability, from yellow (best) to pink (worst). The MAP solution is given in the top left of each panel with 95% confidence intervals (CI) centred on the mean, with the exception of the locking depths which are given with the 95% interquartile range (IQR) centred on the median. The median elevation and GNSS velocities within each profile are shown in grey and as black circles with error bars, respectively.

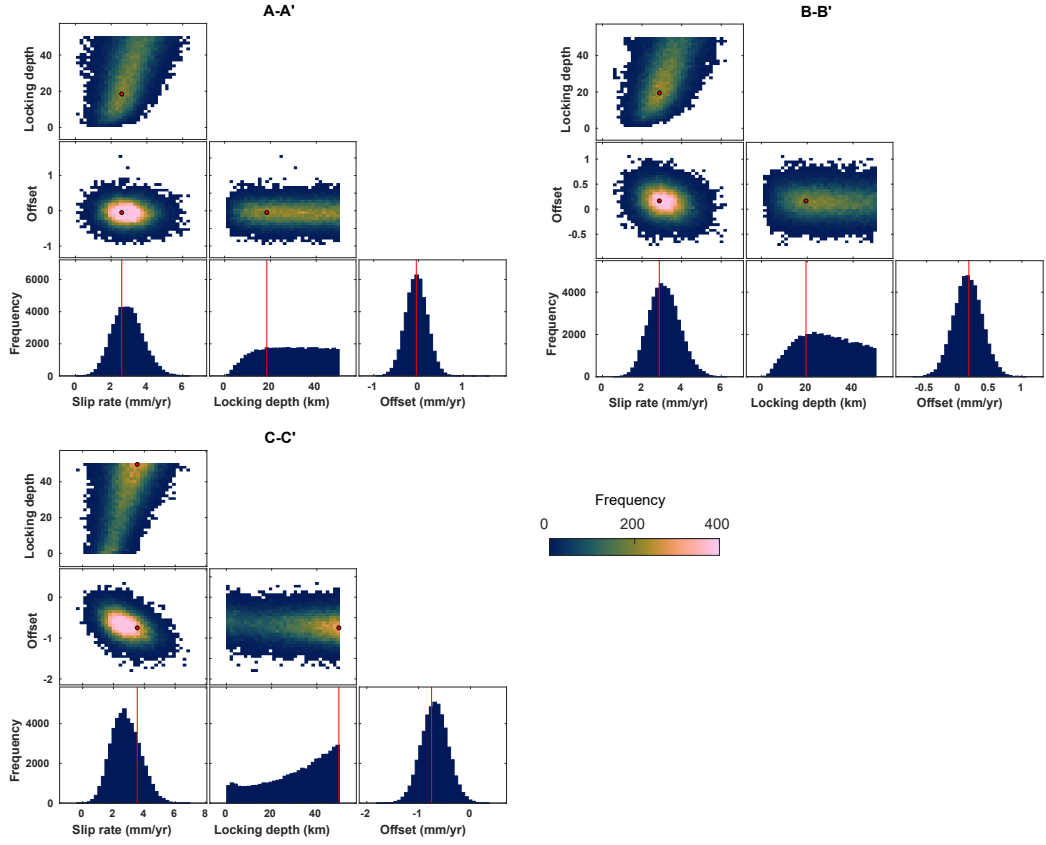


**Figure 9.** Marginal probability distribution for the profiles in Figure 8, including the MAP solution (red line and dot), for the MCMC inversion (48,000 solutions) under the assumption of independent slip rates, locking depths, and offsets for each profile. We assume a uniform prior for all model parameters based upon limits on the values of slip rate (-10–20 mm/yr), locking depth (1–50 km), and offset (-10–10 mm/yr).

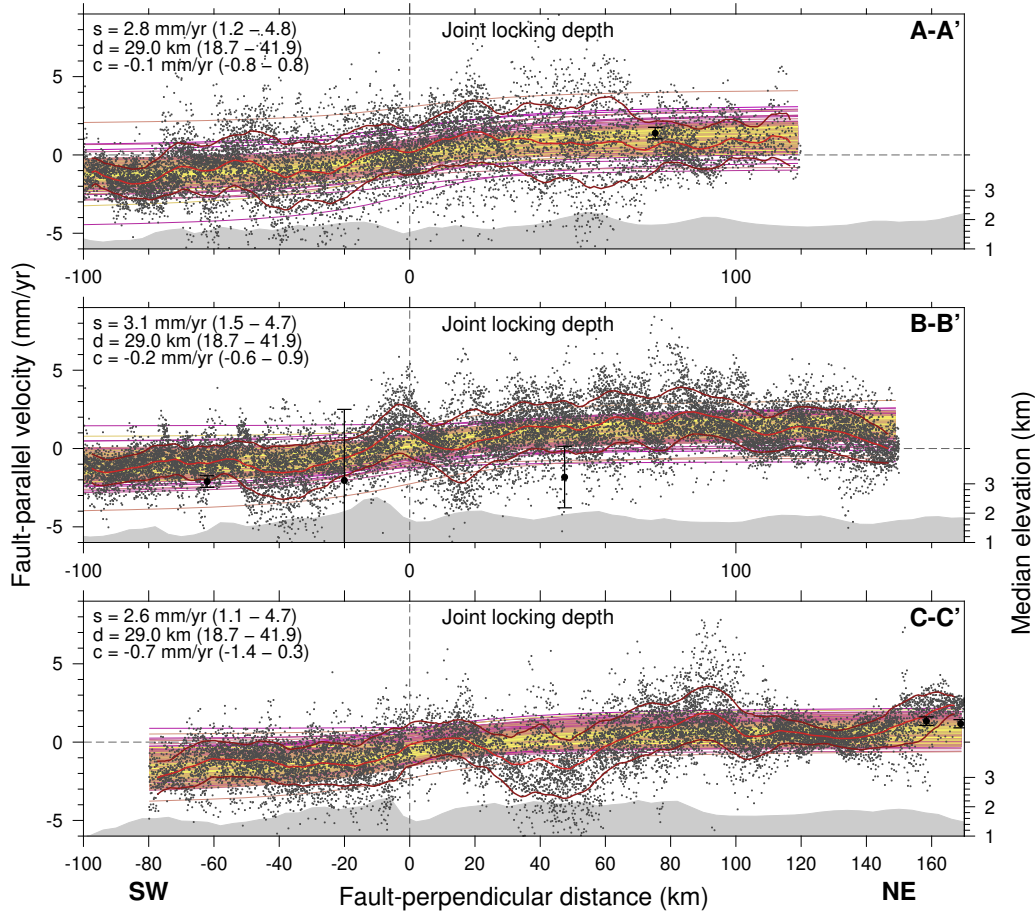


**Figure 10.** Northeast-southwest profiles of fault-parallel (strike direction) velocity (with positive motion to the SE shown by the black dots) relative to the surface trace of the MRF (set at zero distance), from Figure 7, modelled with a joint locking depth and individual slip rates and offsets. The light and dark red lines show the weighted average and weighted standard deviation of the velocities, respectively. A uniformly randomly selected 1% of modelled solutions are shown ranked by the posteriori probability, from yellow (best) to pink (worst). The MAP solution is given in the top left of each panel with 95% confidence intervals (CI) centred on the mean. The median elevation and GNSS velocities within each profile are shown in grey and as black circles with error bars, respectively.

433 locking depth (29.0 km) is now Gaussian, giving a 95% confidence interval of 18.7–41.9 mm/yr.  
 434 This interval only encompasses the individual locking depth estimate for profile B-B' (19.4 km),  
 435 although the joint estimate of 29.0 km is within the 95% IQR for both profiles A-A' and  
 436 B-B'. While not directly comparable, the uncertainties on the joint estimate of locking  
 437 depth are narrower than those on the individual estimates. The distribution appears more  
 438 Gaussian, with a small skew to higher values. While the bounds are more defined than  
 439 the individual estimates, a high kurtosis value of 5.5 (compared to an average of 3.6 for  
 440 the slip rate distributions) indicates long tails on the distribution.

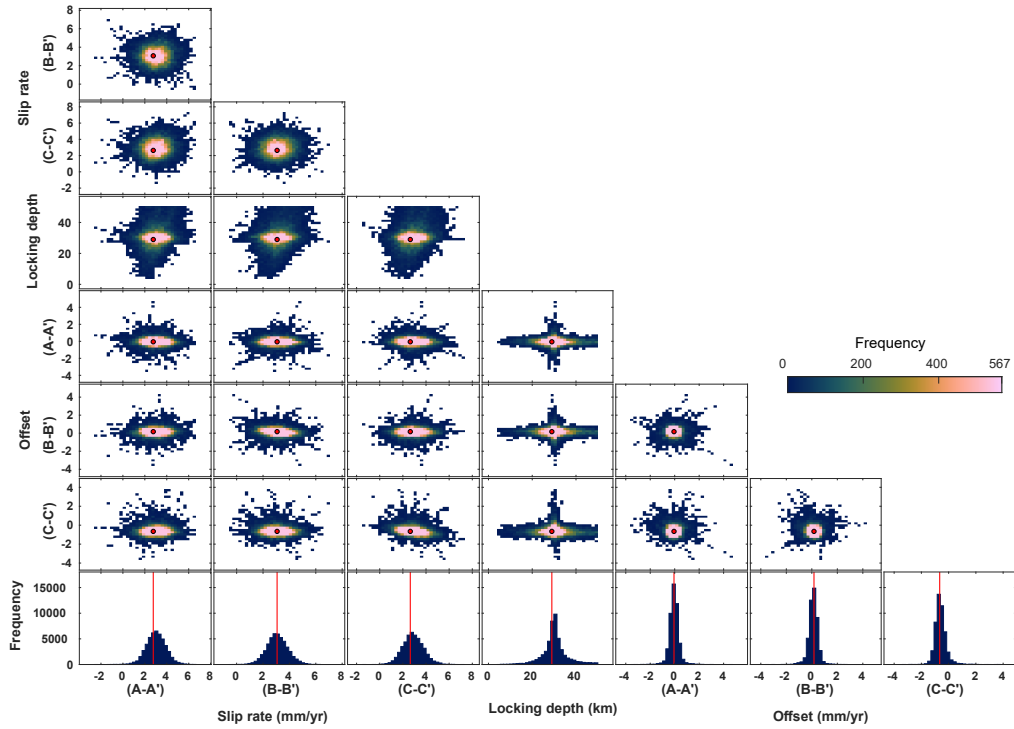


**Figure 11.** Marginal probability distribution for the profiles in Figure 10, including the MAP solution (red line and dot), for the MCMC inversion (48,000 solutions) under the assumption of a single locking depth along strike of the MRF (i.e. a common joint locking depth for all three profiles). We assume a uniform prior for all model parameters based upon limits on the values of slip rate (-10–20 mm/yr), locking depth (1–50 km), and offset (-10–10 mm/yr).

## 5 Discussion

We have resolved a small rate of strain accumulation at the millimeter per year level across spatial distances of 100 km over the Main Recent Fault from 5.5 years of Sentinel-1 InSAR times series. Furthermore, we have placed geodetic bounds for the first time on the depth below which the fault is slipping in this interseismic period. Below we compare our results to previous estimates of interseismic slip rate, discuss the model uncertainties, which remain high despite the large volume of data used here, and also discuss challenges in constraining the locking depth for relatively noisy interseismic InSAR datasets.

### 5.1 Estimation of the Locking Depth

Our results provide the first geodetic estimate for the locking depth of the Main Recent Fault, SW Iran. Our three estimates of locking depth from profiles A-A' (18.4 km), B-B' (19.4 km), and the joint model (29.0 km), all lie within each other's large uncertainties (5.6–48.9 km, 7.1–48.6 km, and 18.7–41.9 km). While the upper limit is poorly constrained for both A-A' and B-B', and C-C' is unbounded within our prior limits, we show that a joint inversion of multiple along-strike profiles with variable strike angles can better constrain the locking depth, both in terms of the upper bound and the width of the uncertainties. The improved upper bound on our joint estimate of the locking depth may be a result of the averaging of the long wavelength trend either side of the fault, which eliminates some unrealistically deep values. Our 95% confidence interval for the joint estimate of 18.7–41.9 km, equal to a standard deviation of 5.8 km, is in line with typical locking depth uncertainties from InSAR (e.g. Karimzadeh et al., 2013; Walters et al., 2011; Karimzadeh et al., 2013), although narrower uncertainties are achievable with higher slip rates (e.g. H. Wang et al., 2009; Fattahi & Amelung, 2016). Calibrated earthquake locations for the MRF from Karasözen et al. (2019) show a maximum centroid depth of roughly 20 km, suggesting that the fault is locked to around this depth. Examining the fault-parallel projected GNSS velocities from Khorrami et al. (2019) shown in Figures 8 and 10, we can see that the local GNSS network lacks suitable station density around the fault trace to capture the velocity gradient, and thus estimate the locking depth.

The poorly constrained upper bounds on the locking depth for profiles A-A' and B-B' suggest that the fit of our screw dislocation model to our fault-parallel velocities is relatively insensitive to the choice of locking depth. Similarly, the MAP estimate of slip rate for C-C' (3.5 mm/yr) is within the  $1\sigma$  uncertainties of the slip rate estimates from A-A' and B-B', despite the large differences in locking depth (49.7 km versus 18.4 km and 19.4 km, respectively).

The wavelength of the velocity gradient across the fault trace is primarily controlled by the locking depth (Equation 5). Most of the strain is accommodated within a distance either side of the fault that is similar to a few times the locking depth. Figure 12 shows the weighted least squares estimates of slip rate for fixed values of locking depth between 1 and 50 km, along with the normalised RMS misfit between the model (Equation 5) and the fault-parallel velocities, for each individual profile and with a joint locking depth as in Figure 11. We weight the least squares with the same variance-covariance matrix as used for the Bayesian analysis. For all three profiles and the joint model, we observe a strong trade-off between the interseismic slip rate on the fault and the locking depth, from 1–1.5 mm/yr at 1 km to 3.4–3.7 mm/yr at 50 km. The magnitude of this trade-off is greatest for locking depths below 10 km. The normalised RMS misfit shows large minimums for profiles A-A' (7–20 km), B-B' (14–35 km), and the joint model (18–50 km). The misfit for C-C' does not define a flat minimum within the 1–50 km locking depth range, in agreement with the unbounded distribution show in Figure 11. Comparing Figure 12 to the a posteriori distributions shown in Figure 9, we can see that the choice of a deeper locking depth has little impact on the overall model fit, and that MAP estimates of locking depth are strongly controlled by the slip rate.

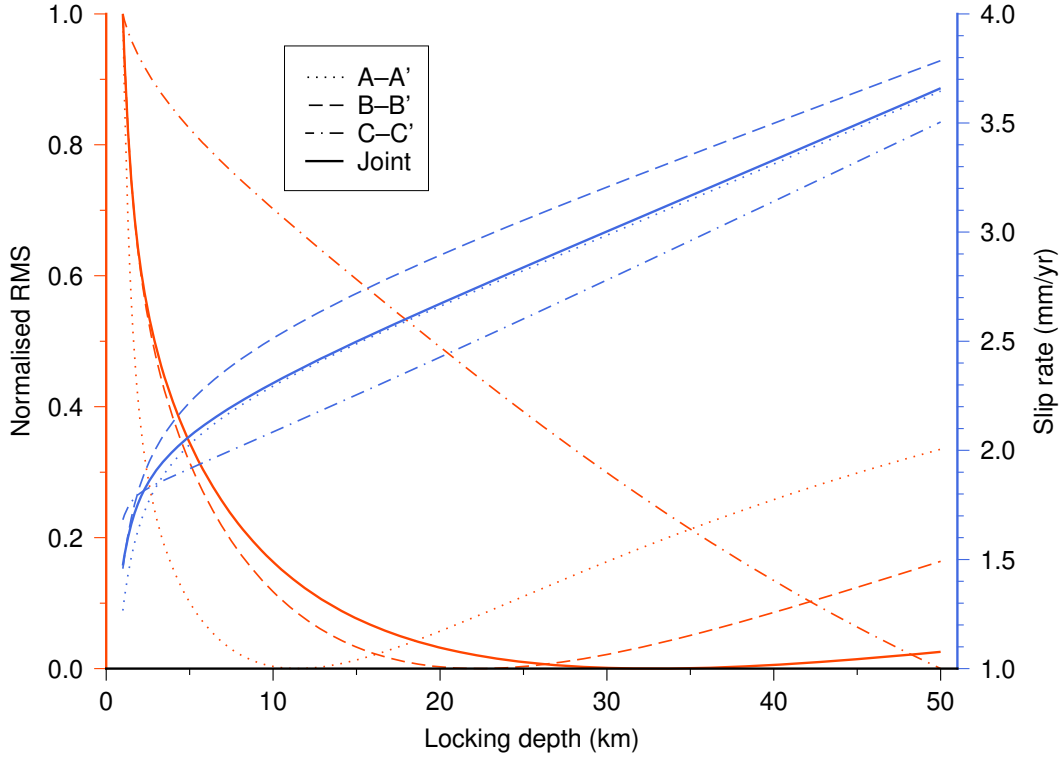


**Figure 12.** Trade-off between the weighted least-squares estimate of slip rate (blue lines) and fixed values of locking depth for profiles A-A' (dotted line), B-B' (dashed line), C-C' (dot-dashed line), and the joint profiles (solid line). In the case of the joint profiles, where we solve for three slips and three offsets, the average slip for all three profiles is shown. The normalised root mean square (RMS) misfit (red lines) between the forward model and the observations highlights a broad minimum for both B-B' and the joint profiles upwards of 15 km, while A-A' gives a lower and narrowed minimum, and C-C' does not reach a minimum.

## 5.2 Previous Estimates of the Interseismic Slip Rate

We produce two MAP estimates of the interseismic slip rate for each profile, using both individual and joint locking depths. These range between 2.6–3.5 mm/yr and 2.6–3.1 mm/yr, respectively. The narrower range for the joint model relates primarily to profile C-C', for which the slip rate for the individual profile is shifted to a higher value by the deep locking depth. The confidence intervals are almost identical between the individual and joint estimates. In both cases, the minimum of the confidence interval is above 0 mm/yr, and so we can be confident that the fault is actively accumulating strain in a right-lateral sense. For the individual profile estimate, we calculate a mean slip rate of  $3.0 \pm 1.0$  mm/yr ( $2\sigma$ ). We do not calculate a mean and uncertainty from the joint slip rates, as the shared locking depth means that these estimates are not independent. However, the range of estimates (2.6–3.1 mm/yr) is in agreement with the average individual rate.

These slip rate estimates are comparable to some of the slowest geodetically observed interseismic slip rates in the literature. Bell et al. (2011) estimated a rate of  $3 \pm 2$  mm/yr for the Manyi fault, Tibet, using 10 ERS images over 5 years to form long-period interferograms. Mousavi et al. (2015) estimated a similar rate of  $4.75 \pm 0.8$  mm/yr for the Shahroud fault, northeast Iran, from 45 Envisat images over a 7 year period. Both studies highlight the importance of the length of the time series over the number of images when resolving slow slip rates. The low slip rate estimate for the Manyi fault was possible partly due to the lack of significant atmospheric noise, both because of low topographic variation along the profile, and because of the arid climate of the high Tibetan Plateau. The latter also allowed for long temporal baseline interferograms with sufficient coherence to obtain reasonable coverage of the tectonic signal, although we note that the velocity field is patchy. Bell et al. (2011) also highlight the difficulty in constraining the locking depth for signals of this magnitude, with their Monte Carlo solutions reaching their limits of 0–40 km. Mousavi et al. (2015) provides a narrower locking depth estimate of  $10 \pm 4$  km (66% CI), although the result is still relatively insensitive to the choice of locking depth in comparison to the choice of slip rate.

Our range of slip rate estimates is in agreement with previous GNSS derived estimates for the Main Recent Fault from Vernant et al. (2004, b) ( $3 \pm 2$  mm/yr), Walpersdorf et al. (2006) (4–6 mm/yr), and Khorrami et al. (2019) (2.7–4 mm/yr), along with the geological/geomorphological-derived estimates from Alipoor et al. (2012) (1.6–3.2 mm/yr) and Copley and Jackson (2006) (2–5 mm/yr). Our estimates are lower than other geological/geomorphological-derived estimates from Talebian and Jackson (2002) (10–17 mm/yr) and Bachmanov et al. (2004) (10 mm/yr), and comparable to the lower end of estimates from Authemayou et al. (2009) (3.5–12.5 mm/yr). Whilst our InSAR results are not entirely independent of the GNSS data, as the GNSS data from Khorrami et al. (2019) are used to constrain the north-south velocities, the InSAR data does provide significant additional constraint. Our new InSAR-derived interseismic slip estimate affirms that the MRF is slipping at a geodetic rate of a few millimeters per year.

The broad range of slip rates estimates from geological and geomorphological methods can be tied to differences in two parameters: the average offset on the fault, and the time over which the offset occurred. Talebian and Jackson (2002), Copley and Jackson (2006), and Alipoor et al. (2012) all use the inception of the MRF as their timescale. Both Talebian and Jackson (2002) and Copley and Jackson (2006) assume an age of 3–5 ma for the MRF, based on the onset of shortening in the Simply Folded Belt of the Zagros, but measure markedly different offsets of 50 km and 10–15 km, respectively. Alipoor et al. (2012) estimate an offset of 16 km on the MRF, and use an initiation time of 5–10 ma based on the timing of slab break-off below the Zagros. Bachmanov et al. (2004) and Authemayou et al. (2009) both measure offsets over a period of thousands of years, the former using the beginning of the Holocene, and the latter using the exposure ages of samples from various geomorphic features. Copley and Jackson (2006) suggest that, based on differ-

ing offsets measured along adjacent fault sections, that either the average slip rate on the MRF varies along strike, or that the onset of faulting was heterogeneous along the length of the fault. In addition, Austermann and Iaffaldano (2013) proposed that the total convergence rate may have decreased by 30% since 5 Ma, which would reduce the slip rate along the MRF. However, the overlap between the lower end of the geological slip rate estimates and the geodetic estimates could suggest that the slip rate on the MRF may have been largely consistent through time.

Our InSAR-derived velocity fields and fault modelling suggest that the component of motion parallel to the tectonic boundary between the Arabian plate and Iran in our study area is localised onto the MRF. We expand on this by calculating the percentage of partitioned strike-slip motion accommodated by the MRF across the northwestern Zagros. We take a subset of GNSS velocities from Khorrami et al. (2019), located either side of the northwestern Zagros (Figure S10), and calculate the difference between the weighted mean velocities. We assume a single range-strike of  $310^\circ$  and decompose the velocity difference into range-parallel and range-perpendicular components with values of 4.3 mm/yr and 5.3 mm/yr, respectively. Our interseismic slip rate estimate of  $3 \pm 1$  mm/yr for the MRF would account for 46–93% of the overall strike-slip component. At the upper end, this suggests that movement along the MRF alone is sufficient to account for the strike-slip component across this part of the Zagros. At the lower end, this would suggest that strike-slip motion also occurs on adjacent faults, either outside of our study area or with slip rates below our sensing limit, or that a component of the range-parallel motion is accommodated by off-fault deformation. This is in agreement with block modelling from Khorrami et al. (2019), who estimate 2.7–4 mm/yr of fault-parallel motion along the MRF, and a smaller 0.5 mm/yr fault-parallel component in the Frontal fault zone, which shares a similar strike to the MRF between  $46^\circ$ – $50^\circ$  E. The localisation of strike-slip motion paired with distributed thrust faulting has also been observed in the Qilian Shan, northeastern Tibetan Plateau (Allen et al., 2017). Allen et al. (2017) suggest that this arrangement, previously observed in oblique oceanic subduction zones (McCaffrey et al., 2000), may apply generally to oblique convergence zones. Slip may have become localised on the MRF because of an existing weakness in the form of the Main Zagros Thrust Fault, the trace of which the MRF partially inherited.

The localisation of slip on the MRF poses a greater risk of higher magnitude earthquakes than if the deformation was distributed on smaller faults. Given the simplistic scenario that all accumulated strain on the MRF is released seismically by only  $M_w$  7 earthquakes, we can calculate an average recurrence interval for a  $M_w$  7 earthquake similar to the 1909 Dorud earthquake (Ambraseys & Moinfar, 1973) occurring on the fault (e.g. Walters et al., 2014) Assuming an interseismic slip rate of 2–4 mm/yr, on a vertical strike slip fault with a locking depth of 22 km (average of our estimates from A-A', B-B', and the joint model), a shear modulus of  $3 \times 10^{10}$  Pa and a slip-to-length ratio of  $3 \times 10^{-5}$ , we estimate a recurrence time of 315–631 years.

Our estimates for both the interseismic slip rate and the locking depth of the MRF must be kept in the context of our modelling limitations. The poor signal-to-noise ratio of our tectonic signal limited the number of model parameters we were able to constrain. Our screw dislocation model (Equation 5) assumes that all interseismic slip can be reasonably approximated as being localised onto a single vertical plane. Source modelling of the 2006  $M_w$  6.1 Silakhour earthquake (Peyret et al., 2008; Ghods et al., 2012), which ruptured two segments of the MRF, suggests that the dip of the MRF may be as low as  $60^\circ$ , in agreement with teleseismic crustal imaging (Dashti et al., 2020), and that the shear zone is located up to 10 km north of the fault trace. We also assume identical rheological parameters either side of the MRF, which in reality forms the boundary between the High Zagros and the Central Iranian Plateau (Allen et al., 2013). Future work may incorporate longer InSAR time series, including images for other InSAR satel-

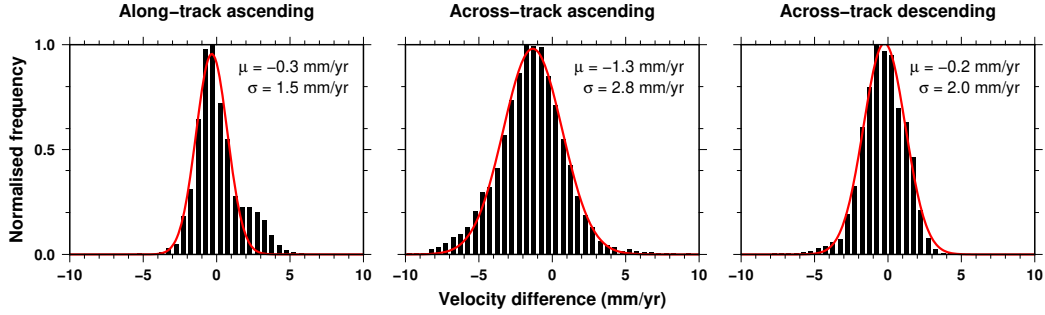


**Figure 13.** Histograms for the difference between projected horizontal velocities in frame overlaps along ascending tracks (174A-N and 174A-S), across ascending tracks (174A-N, 174A-S, and 101A), and across descending tracks (006D and 108D). Best fitting Gaussians are shown in red, along with their mean,  $\mu$ , and standard deviation,  $\sigma$ .

597 lites such as Envisat and ERS, to improve the signal-to-noise ratio and to attempt to  
 598 model a more complex fault geometry and rheological contrasts (e.g. Jolivet et al., 2008)

### 599 5.3 Modelling Velocity Uncertainties

600 Given our low interseismic slip rate estimate for the MRF, one of the slowest InSAR-  
 601 derived fault slips rates published so far, it is valuable to assess the uncertainties asso-  
 602 ciated with our InSAR velocities. Bootstrapped estimates of the InSAR velocity uncer-  
 603 tainty have been shown to decrease with increasing time series length (Morishita et al.,  
 604 2020), with a 2 mm/yr standard deviation achievable with 1.4 and 1.8 years of 6 and 12  
 605 day acquisitions, respectively. Uncertainties for combined GNSS and InSAR velocities,  
 606 however, may level off around 2–3 mm/yr as the uncertainty on the GNSS velocities be-  
 607 comes dominant (Weiss et al., 2020). As another estimate of the uncertainties, and to  
 608 examine the effectiveness of the InSAR referencing, we calculate the difference in veloc-  
 609 ities (Figure 13) between overlapping frames (Walters et al., 2014). We assume that all  
 610 velocities are purely horizontal by dividing by the sine of the incidence angle and then  
 611 multiplying by the incidence angle at the centre of each frame. The frame overlap be-  
 612 tween 174A-N and 174A-S covers part of the Sarpol earthquake cluster, meaning our as-  
 613 sumption of only horizontal velocities is poor. Despite this, we still observe  $1\sigma$  uncer-  
 614 tainties less than 3 mm/yr, inline with those observed in previous studies (Hussain, Hooper,  
 615 et al., 2016; Liu et al., 2018; Weiss et al., 2020). This implies that the referencing of the  
 616 InSAR LOS velocities to a Eurasia-fixed frame has been reasonably successful. These  
 617 standard deviations can be considered as  $\sqrt{2} \times$  the velocity uncertainty for each frame.  
 618 This gives a  $1\sigma$  uncertainty of 1.36 mm/yr for 006D and 108D. For the ascending frames  
 619 we take the mean of the along-track and across-track values, giving a  $1\sigma$  uncertainty of  
 620 1.41 mm/yr for 174A and 101A.

## 621 6 Conclusion

622 We have used over 5.5 years of Sentinel-1 SAR images across two ascending and  
 623 two descending tracks to produce the first InSAR-derived estimate of interseismic slip  
 624 rate for the Main Recent Fault, SW Iran. We combine InSAR LOS velocities with GNSS  
 625 to estimate the fault-parallel velocity for three across-fault profiles which we model both  
 626 individually and together to better constrain the fault parameters. Our estimated rate  
 627 of  $3.0 \pm 1.0$  mm/yr for the MRF between  $47^\circ$  E and  $50^\circ$  E is in agreement with previ-  
 628 ous geodetic rates from GNSS studies, and is one of the slowest interseismic slip rates  
 629 measured using InSAR. We provide the first estimate of the locking depth of the fault

630 (18–30 km) while highlighting the difficulties of modelling tectonic signals close to the  
 631 current InSAR noise level. We show that the strike-slip component of the overall plate  
 632 motion in our study area is localised onto the MRF, with a slip rate of  $3.0\pm 1.0$  mm/yr  
 633 accounting for 46–93% of the strike-slip component across the western Zagros. Our re-  
 634 sults show that the MRF is an important major crustal structure that shows a locali-  
 635 sation of strain at depth and which accommodates an appreciable portion of the rela-  
 636 tive motion between Arabia and Eurasia.

### 637 Acknowledgments

638 We thank Milan Lazecky and Yasser Maghsoudi Mehrani for assistance with the LiC-  
 639 SAR processing tools, and Yu Morishita for assistance with the LiCSBAS software. Fig-  
 640 ures were made using the Generic Mapping Tools (GMT, Wessel et al., 2013).

641 Andrew Watson is supported through a PhD studentship from the Royal Society  
 642 (RGF\R1\180076). This work is supported by the UK Natural Environment Research  
 643 Council (NERC) through the Centre for the Observation and Modelling of Earthquakes,  
 644 Volcanoes and Tectonics (COMET, <http://comet.nerc.ac.uk>). This work is also supported  
 645 by NERC through the Looking into the Continents from Space (LiCS) large Grant (NE/K010867/1).  
 646 John Elliott acknowledges support from the Royal Society through a University Research  
 647 Fellowship (UF150282).

648 The Sentinel-1 InSAR data are copyrighted by the European Space Agency and  
 649 provided freely through the Copernicus Open Access Hub (<https://scihub.copernicus.eu/>).  
 650 Sentinel-1 InSAR data are also freely distributed by the Alaska Satellite Facility (<https://asf.alaska.edu/>).  
 651 Processed SAR images, wrapped interferograms, and unwrapped interferograms used in  
 652 this work can be found on the COMET-LiCS Sentinel-1 InSAR portal ([https://comet.nerc.ac.uk/COMET-  
 653 LiCS-portal/](https://comet.nerc.ac.uk/COMET-LiCS-portal/)). Information on accessing the LiCSBAS software can be found in Morishita  
 654 et al. (2020). Information on accessing the GACOS atmospheric corrections can be found  
 655 in Yu, Li, Penna, and Crippa (2018).

### 656 References

- 657 Aghajany, S. H., Voosoghi, B., & Yazdian, A. (2017). Estimation of north Tabriz  
 658 fault parameters using neural networks and 3D tropospherically corrected sur-  
 659 face displacement field. *Geomatics, Natural Hazards and Risk*, *8*(2), 918–932.
- 660 Alipoor, R., Zaré, M., & Ghassemi, M. R. (2012). Inception of activity and slip rate  
 661 on the Main Recent Fault of Zagros Mountains, Iran. *Geomorphology*, *175*, 86–  
 662 97.
- 663 Allen, M., Jackson, J., & Walker, R. (2004). Late Cenozoic reorganization of the  
 664 Arabia-Eurasia collision and the comparison of short-term and long-term de-  
 665 formation rates. *Tectonics*, *23*(2).
- 666 Allen, M., Saville, C., Blanc, E.-P., Talebian, M., & Nissen, E. (2013). Orogenic  
 667 plateau growth: Expansion of the Turkish-Iranian Plateau across the Zagros  
 668 fold-and-thrust belt. *Tectonics*, *32*(2), 171–190.
- 669 Allen, M., Walters, R. J., Song, S., Saville, C., De Paola, N., Ford, J., ... Sun, W.  
 670 (2017). Partitioning of oblique convergence coupled to the fault locking be-  
 671 havior of fold-and-thrust belts: Evidence from the Qilian Shan, northeastern  
 672 Tibetan Plateau. *Tectonics*, *36*(9), 1679–1698.
- 673 Ambraseys, N., & Moinfar, A. (1973). The seismicity of Iran, The Silakhor  
 674 (Lurestan) earthquake of 23rd. January 1909. *Annals of Geophysics*, *26*(4),  
 675 659–678.
- 676 Aslan, G., Lasserre, C., Cakir, Z., Ergintav, S., Özarparci, S., Dogan, U., ... Renard,  
 677 F. (2019). Shallow creep along the 1999 Izmit Earthquake rupture (Turkey)  
 678 from GPS and high temporal resolution interferometric synthetic aperture  
 679 radar data (2011–2017). *Journal of Geophysical Research: Solid Earth*, *124*(2),

- 680 2218–2236.
- 681 Austermann, J., & Iaffaldano, G. (2013). The role of the Zagros orogeny in slowing  
682 down Arabia-Eurasia convergence since ~ 5 Ma. *Tectonics*, *32*(3), 351–363.
- 683 Authemayou, C., Bellier, O., Chardon, D., Benedetti, L., Malekzade, Z., Claude, C.,  
684 ... Abbassi, M. R. (2009). Quaternary slip-rates of the Kazerun and the Main  
685 Recent Faults: active strike-slip partitioning in the Zagros fold-and-thrust belt.  
686 *Geophysical Journal International*, *178*(1), 524–540.
- 687 Bachmanov, D., Trifonov, V., Hessami, K. T., Kozhurin, A., Ivanova, T., Rogozhin,  
688 E., ... Jamali, F. (2004). Active faults in the Zagros and central Iran.  
689 *Tectonophysics*, *380*(3-4), 221–241.
- 690 Barnhart, W. D., Brengman, C. M., Li, S., & Peterson, K. E. (2018). Ramp-flat  
691 basement structures of the Zagros Mountains inferred from co-seismic slip and  
692 afterslip of the 2017 Mw 7.3 Darbandikhan, Iran/Iraq earthquake. *Earth and  
693 Planetary Science Letters*, *496*, 96–107.
- 694 Bell, M., Elliott, J., & Parsons, B. (2011). Interseismic strain accumulation across  
695 the Manyi fault (Tibet) prior to the 1997 Mw 7.6 earthquake. *Geophysical re-  
696 search letters*, *38*(24).
- 697 Biggs, J., Wright, T., Lu, Z., & Parsons, B. (2007). Multi-interferogram method for  
698 measuring interseismic deformation: Denali Fault, Alaska. *Geophysical Journal  
699 International*, *170*(3), 1165–1179.
- 700 Bird, P. (2003). An updated digital model of plate boundaries. *Geochemistry, Geo-  
701 physics, Geosystems*, *4*(3).
- 702 Chen, C. W., & Zebker, H. A. (2000). Network approaches to two-dimensional phase  
703 unwrapping: intractability and two new algorithms. *JOSA A*, *17*(3), 401–414.
- 704 Chen, C. W., & Zebker, H. A. (2001). Two-dimensional phase unwrapping with  
705 use of statistical models for cost functions in nonlinear optimization. *JOSA A*,  
706 *18*(2), 338–351.
- 707 Chen, C. W., & Zebker, H. A. (2002). Phase unwrapping for large SAR interfero-  
708 grams: Statistical segmentation and generalized network models. *IEEE Trans-  
709 actions on Geoscience and Remote Sensing*, *40*(8), 1709–1719.
- 710 Copley, A., & Jackson, J. (2006). Active tectonics of the Turkish-Iranian plateau.  
711 *Tectonics*, *25*(6).
- 712 Dashti, F., Lucente, F. P., Motaghi, K., Bianchi, I., Najafi, M., Govoni, A., & Sha-  
713 banian, E. (2020). Crustal scale imaging of the Arabia-Central Iran collision  
714 boundary across the Zagros suture zone, west of Iran. *Geophysical Research  
715 Letters*, *47*(8), e2019GL085921.
- 716 Doin, M.-P., Guillaso, S., Jolivet, R., Lasserre, C., Lodge, F., Ducret, G., &  
717 Grandin, R. (2011). Presentation of the small baseline NSBAS processing  
718 chain on a case example: the Etna deformation monitoring from 2003 to 2010  
719 using Envisat data. In *Proceedings of the fringe symposium* (pp. 3434–3437).
- 720 Efron, B., & Tibshirani, R. (1986). Bootstrap methods for standard errors, confi-  
721 dence intervals, and other measures of statistical accuracy. *Statistical science*,  
722 *54*–75.
- 723 Farr, T. G., Rosen, P. A., Caro, E., Crippen, R., Duren, R., Hensley, S., ... others  
724 (2007). The shuttle radar topography mission. *Reviews of geophysics*, *45*(2).
- 725 Fattahi, H., & Amelung, F. (2016). InSAR observations of strain accumulation and  
726 fault creep along the Chaman Fault system, Pakistan and Afghanistan. *Geo-  
727 physical Research Letters*, *43*(16), 8399–8406.
- 728 Fialko, Y. (2006). Interseismic strain accumulation and the earthquake potential on  
729 the southern San Andreas fault system. *Nature*, *441*(7096), 968–971.
- 730 Ghods, A., Rezapour, M., Bergman, E., Mortezaejad, G., & Talebian, M. (2012).  
731 Relocation of the 2006 Mw 6.1 Silakhour, Iran, earthquake sequence: details  
732 of fault segmentation on the Main Recent Fault. *Bulletin of the Seismological  
733 Society of America*, *102*(1), 398–416.

- 734 Goodman, J., & Weare, J. (2010). Ensemble samplers with affine invariance. *Com-*  
735 *munications in applied mathematics and computational science*, 5(1), 65–80.
- 736 Goto, H., Toyomasu, A., & Sawada, S. (2019). Delayed subevents during the Mw 6.2  
737 first shock of the 2016 Kumamoto, Japan, earthquake. *Journal of Geophysical*  
738 *Research: Solid Earth*, 124(12), 13112–13123.
- 739 Hatzfeld, D., & Molnar, P. (2010). Comparisons of the kinematics and deep struc-  
740 tures of the Zagros and Himalaya and of the Iranian and Tibetan plateaus and  
741 geodynamic implications. *Reviews of Geophysics*, 48(2).
- 742 Hessami, K., Nilforoushan, F., & Talbot, C. J. (2006). Active deformation within  
743 the Zagros mountains deduced from GPS measurements. *Journal of the Geo-*  
744 *logical Society*, 163(1), 143–148.
- 745 Hussain, E., Hooper, A., Wright, T. J., Walters, R. J., & Bekaert, D. P. (2016).  
746 Interseismic strain accumulation across the central North Anatolian Fault from  
747 iteratively unwrapped InSAR measurements. *Journal of Geophysical Research:*  
748 *Solid Earth*, 121(12), 9000–9019.
- 749 Hussain, E., Wright, T. J., Walters, R. J., Bekaert, D., Hooper, A., & Houseman,  
750 G. A. (2016). Geodetic observations of postseismic creep in the decade af-  
751 ter the 1999 Izmit earthquake, Turkey: Implications for a shallow slip deficit.  
752 *Journal of Geophysical Research: Solid Earth*, 121(4), 2980–3001.
- 753 Hussain, E., Wright, T. J., Walters, R. J., Bekaert, D. P., Lloyd, R., & Hooper, A.  
754 (2018). Constant strain accumulation rate between major earthquakes on the  
755 North Anatolian Fault. *Nature communications*, 9(1), 1–9.
- 756 Jolivet, R., Cattin, R., Chamot-Rooke, N., Lasserre, C., & Peltzer, G. (2008). Thin-  
757 plate modeling of interseismic deformation and asymmetry across the alty  
758 tagh fault zone. *Geophysical Research Letters*, 35(2).
- 759 Jolivet, R., Lasserre, C., Doin, M.-P., Peltzer, G., Avouac, J.-P., Sun, J., & Dailu,  
760 R. (2013). Spatio-temporal evolution of aseismic slip along the Haiyuan fault,  
761 China: Implications for fault frictional properties. *Earth and Planetary Science*  
762 *Letters*, 377, 23–33.
- 763 Karasözen, E., Nissen, E., Bergman, E. A., & Ghods, A. (2019). Seismotectonics of  
764 the Zagros (Iran) from orogen-wide, calibrated earthquake relocations. *Journal*  
765 *of Geophysical Research: Solid Earth*, 124(8), 9109–9129.
- 766 Karimzadeh, S., Cakir, Z., Osmanoglu, B., Schmalzle, G., Miyajima, M., Amiraslan-  
767 zadeh, R., & Djamour, Y. (2013). Interseismic strain accumulation across the  
768 North Tabriz Fault (NW Iran) deduced from InSAR time series. *Journal of*  
769 *Geodynamics*, 66, 53–58.
- 770 Khorrami, F., Vernant, P., Masson, F., Nilfouroushan, F., Mousavi, Z., Nankali, H.,  
771 ... others (2019). An up-to-date crustal deformation map of Iran using in-  
772 tegrated campaign-mode and permanent GPS velocities. *Geophysical Journal*  
773 *International*.
- 774 Kreemer, C., Blewitt, G., & Klein, E. C. (2014). A geodetic plate motion and  
775 Global Strain Rate Model. *Geochemistry, Geophysics, Geosystems*, 15(10),  
776 3849–3889.
- 777 Liu, C., Ji, L., Zhu, L., & Zhao, C. (2018). InSAR-constrained interseismic deforma-  
778 tion and potential seismogenic asperities on the Altyn Tagh fault at 91.5–95 E,  
779 Northern Tibetan Plateau. *Remote Sensing*, 10(6), 943.
- 780 Lv, X., Amelung, F., Shao, Y., Ye, S., Liu, M., & Xie, C. (2020). Rheology of  
781 the Zagros Lithosphere from Post-Seismic Deformation of the 2017 Mw 7.3  
782 Kermanshah, Iraq, Earthquake. *Remote Sensing*, 12(12), 2032.
- 783 McCaffrey, R., Zwick, P. C., Bock, Y., Prawirodirdjo, L., Genrich, J. F., Stevens,  
784 C. W., ... Subarya, C. (2000). Strain partitioning during oblique plate  
785 convergence in northern Sumatra: Geodetic and seismologic constraints and  
786 numerical modeling. *Journal of Geophysical Research: Solid Earth*, 105(B12),  
787 28363–28376.
- 788 McClusky, S., Reilinger, R., Mahmoud, S., Ben Sari, D., & Tealeb, A. (2003). GPS

- 789 constraints on Africa (Nubia) and Arabia plate motions. *Geophysical Journal*  
790 *International*, 155(1), 126–138.
- 791 Morishita, Y. (2021). Nationwide urban ground deformation monitoring in Japan  
792 using Sentinel-1 LiCSAR products and LiCSBAS. *Progress in Earth and Plan-*  
793 *etary Science*, 8(1), 1–23.
- 794 Morishita, Y., Lazecky, M., Wright, T. J., Weiss, J. R., Elliott, J. R., & Hooper,  
795 A. (2020). LiCSBAS: An open-source InSAR time series analysis package  
796 integrated with the LiCSAR automated Sentinel-1 InSAR processor. *Remote*  
797 *Sensing*, 12(3), 424.
- 798 Mousavi, Z., Fattahi, M., Khatib, M., Talebian, M., Pathier, E., Walpersdorf, A.,  
799 ... others (2021). Constant slip-rate on the Doruneh strike-slip fault, Iran,  
800 averaged over Late Pleistocene, Holocene, and decadal timescales. *Tectonics*,  
801 e2020TC006256.
- 802 Mousavi, Z., Pathier, E., Walker, R., Walpersdorf, A., Tavakoli, F., Nankali, H., ...  
803 Doin, M.-P. (2015). Interseismic deformation of the Shahroud fault system  
804 (NE Iran) from space-borne radar interferometry measurements. *Geophysical*  
805 *Research Letters*, 42(14), 5753–5761.
- 806 Murray, K. D., Bekaert, D. P., & Lohman, R. B. (2019). Tropospheric corrections  
807 for InSAR: Statistical assessments and applications to the Central United  
808 States and Mexico. *Remote Sensing of Environment*, 232, 111326.
- 809 Niassarifard, M., Shabaniyan, E., Azad, S. S., & Madanipour, S. (2021). New tectonic  
810 configuration in NW Iran: Intracontinental dextral shear between NW Iran  
811 and SE Anatolia. *Tectonophysics*, 228886.
- 812 Nippress, S. E., Heyburn, R., & Walters, R. (2017). The 2008 and 2012 Moosiyan  
813 earthquake sequences: Rare insights into the role of strike slip and thrust fault-  
814 ing within the simply folded belt (Iran). *Bulletin of the Seismological Society*  
815 *of America*, 107(4), 1625–1641.
- 816 Nissen, E., Ghods, A., Karasözen, E., Elliott, J. R., Barnhart, W. D., Bergman,  
817 E. A., ... others (2019). The 12 November 2017 Mw 7.3 Ezgeleh–Sarpolzahab  
818 (Iran) earthquake and active tectonics of the Lurestan arc. *Journal of Geo-*  
819 *physical Research: Solid Earth*.
- 820 Nissen, E., Tatar, M., Jackson, J. A., & Allen, M. B. (2011). New views on earth-  
821 quake faulting in the Zagros fold-and-thrust belt of Iran. *Geophysical Journal*  
822 *International*, 186(3), 928–944.
- 823 Okada, Y. (1985). Surface deformation due to shear and tensile faults in a half-  
824 space. *Bulletin of the seismological society of America*, 75(4), 1135–1154.
- 825 Parker, A. L., Biggs, J., Walters, R. J., Ebmeier, S. K., Wright, T. J., Teanby, N. A.,  
826 & Lu, Z. (2015). Systematic assessment of atmospheric uncertainties for In-  
827 SAR data at volcanic arcs using large-scale atmospheric models: Application  
828 to the Cascade volcanoes, United States. *Remote Sensing of Environment*,  
829 170, 102–114.
- 830 Peyret, M., Djamour, Y., Hessami, K., Regard, V., Bellier, O., Vernant, P., ... oth-  
831 ers (2009). Present-day strain distribution across the Minab-Zendan-Palami  
832 fault system from dense GPS transects. *Geophysical Journal International*,  
833 179(2), 751–762.
- 834 Peyret, M., Rolandone, F., Dominguez, S., Djamour, Y., & Meyer, B. (2008). Source  
835 model for the Mw 6.1, 31 March 2006, Chalan-Chulan earthquake (Iran) from  
836 InSAR. *Terra Nova*, 20(2), 126–133.
- 837 Rizza, M., Vernant, P., Ritz, J.-F., Peyret, M., Nankali, H., Nazari, H., ... others  
838 (2013). Morphotectonic and geodetic evidence for a constant slip-rate over the  
839 last 45 kyr along the Tabriz fault (Iran). *Geophysical Journal International*,  
840 193(3), 1083–1094.
- 841 Savage, J. (2000). Viscoelastic-coupling model for the earthquake cycle driven from  
842 below. *Journal of Geophysical Research: Solid Earth*, 105(B11), 25525–25532.
- 843 Savage, J., & Burford, R. (1973). Geodetic determination of relative plate motion in

- 844 central California. *Journal of Geophysical Research*, *78*(5), 832–845.
- 845 Savage, J., & Prescott, W. (1978). Asthenosphere readjustment and the earthquake  
846 cycle. *Journal of Geophysical Research: Solid Earth*, *83*(B7), 3369–3376.
- 847 Sepahvand, M., Yaminifard, F., Tatar, M., & Abbassi, M. (2012). Aftershocks study  
848 of the 2006 Silakhur earthquake (Zagros, Iran): seismological evidences for a  
849 pull-apart basin along the Main Recent Fault, Doroud segments. *Journal of*  
850 *seismology*, *16*(2), 233–251.
- 851 Smith-Konter, B., & Sandwell, D. (2009). Stress evolution of the San Andreas fault  
852 system: Recurrence interval versus locking depth. *Geophysical Research Let-*  
853 *ters*, *36*(13).
- 854 Su, Z., Wang, E.-C., Hu, J.-C., Talebian, M., & Karimzadeh, S. (2016). Quantifying  
855 the termination mechanism along the North Tabriz-North Mishu fault zone of  
856 northwestern Iran via small baseline PS-InSAR and GPS decomposition. *IEEE*  
857 *Journal of Selected Topics in Applied Earth Observations and Remote Sensing*,  
858 *10*(1), 130–144.
- 859 Szeliga, W., & Bilham, R. (2017). New constraints on the mechanism and rupture  
860 area for the 1905 Mw 7.8 Kangra Earthquake, Northwest Himalaya. *Bulletin of*  
861 *the Seismological Society of America*, *107*(5), 2467–2479.
- 862 Talebian, M., & Jackson, J. (2002). Offset on the Main Recent Fault of NW Iran  
863 and implications for the late Cenozoic tectonics of the Arabia–Eurasia collision  
864 zone. *Geophysical Journal International*, *150*(2), 422–439.
- 865 Talebian, M., & Jackson, J. (2004). A reappraisal of earthquake focal mechanisms  
866 and active shortening in the Zagros mountains of Iran. *Geophysical Journal In-*  
867 *ternational*, *156*(3), 506–526.
- 868 Tavakoli, F., Walpersdorf, A., Authemayou, C., Nankali, H., Hatzfeld, D., Tatar,  
869 M., ... Cotte, N. (2008). Distribution of the right-lateral strike-slip motion  
870 from the Main Recent Fault to the Kazerun Fault System (Zagros, Iran): Ev-  
871 idence from present-day GPS velocities. *Earth and Planetary Science Letters*,  
872 *275*(3-4), 342–347.
- 873 Tchalenko, J., & Braud, J. (1974). Seismicity and structure of the Zagros (Iran):  
874 the Main Recent Fault between 33 and 35 N. *Philosophical Transactions of*  
875 *the Royal Society of London. Series A, Mathematical and Physical Sciences*,  
876 *277*(1262), 1–25.
- 877 Tesson, J., Benedetti, L., Godard, V., Novaes, C., Fleury, J., & Team, A. (2021).  
878 Slip rate determined from cosmogenic nuclides on normal-fault facets. *Geology*,  
879 *49*(1), 66–70.
- 880 Thatcher, W. (1983). Nonlinear strain build-up and the earthquake cycle on the San  
881 Andreas fault. *Journal of Geophysical Research: Solid Earth*, *88*(B7), 5893–  
882 5902.
- 883 Tong, X., Sandwell, D., & Smith-Konter, B. (2013). High-resolution interseismic  
884 velocity data along the San Andreas Fault from GPS and InSAR. *Journal of*  
885 *Geophysical Research: Solid Earth*, *118*(1), 369–389.
- 886 Vernant, P., & Chery, J. (2006). Low fault friction in Iran implies localized defor-  
887 mation for the Arabia–Eurasia collision zone. *Earth and Planetary Science Let-*  
888 *ters*, *246*(3-4), 197–206.
- 889 Vernant, P., Nilforoushan, F., Hatzfeld, D., Abbassi, M., Vigny, C., Masson, F., ...  
890 others (2004). Present-day crustal deformation and plate kinematics in the  
891 Middle East constrained by GPS measurements in Iran and northern Oman.  
892 *Geophysical Journal International*, *157*(1), 381–398.
- 893 Walker, R. T., Talebian, M., Saiffiori, S., Sloan, R. A., Rasheedi, A., MacBean, N.,  
894 & Ghassemi, A. (2010). Active faulting, earthquakes, and restraining bend  
895 development near Kerman city in southeastern Iran. *Journal of Structural*  
896 *Geology*, *32*(8), 1046–1060.
- 897 Walpersdorf, A., Hatzfeld, D., Nankali, H., Tavakoli, F., Nilforoushan, F., Tatar,  
898 M., ... Masson, F. (2006). Difference in the GPS deformation pattern of

- 899 North and Central Zagros (Iran). *Geophysical Journal International*, 167(3),  
900 1077–1088.
- 901 Walters, R., Elliott, J., Li, Z., & Parsons, B. (2013). Rapid strain accumulation on  
902 the Ashkabad fault (Turkmenistan) from atmosphere-corrected InSAR. *Journal*  
903 *of Geophysical Research: Solid Earth*, 118(7), 3674–3690.
- 904 Walters, R., Holley, R., Parsons, B., & Wright, T. (2011). Interseismic strain accu-  
905 mulation across the North Anatolian Fault from Envisat InSAR measurements.  
906 *Geophysical research letters*, 38(5).
- 907 Walters, R., Parsons, B., & Wright, T. (2014). Constraining crustal velocity fields  
908 with InSAR for Eastern Turkey: Limits to the block-like behavior of Eastern  
909 Anatolia. *Journal of Geophysical Research: Solid Earth*, 119(6), 5215–5234.
- 910 Wang, H., Wright, T., & Biggs, J. (2009). Interseismic slip rate of the northwestern  
911 Xianshuihe fault from InSAR data. *Geophysical Research Letters*, 36(3).
- 912 Wang, K., & Bürgmann, R. (2020). Probing fault frictional properties during af-  
913 terslip updip and downdip of the 2017 Mw 7.3 Sarpol-e Zahab earthquake  
914 with space geodesy. *Journal of Geophysical Research: Solid Earth*, 125(11),  
915 e2020JB020319.
- 916 Wegnüller, U., Werner, C., Strozzi, T., Wiesmann, A., Frey, O., & Santoro, M.  
917 (2016). Sentinel-1 support in the GAMMA software. *Procedia Computer*  
918 *Science*, 100, 1305–1312.
- 919 Weiss, J. R., Walters, R. J., Morishita, Y., Wright, T. J., Lazecky, M., Wang, H.,  
920 ... others (2020). High-resolution surface velocities and strain for Anato-  
921 lia from Sentinel-1 InSAR and GNSS data. *Geophysical Research Letters*,  
922 e2020GL087376.
- 923 Werner, C., Wegmüller, U., Strozzi, T., & Wiesmann, A. (2000). Gamma SAR  
924 and interferometric processing software. In *Proceedings of the ers-envisat sym-*  
925 *posium, gothenburg, sweden* (Vol. 1620, p. 1620).
- 926 Wessel, P., Smith, W. H., Scharroo, R., Luis, J., & Wobbe, F. (2013). Generic map-  
927 ping tools: improved version released. *Eos, Transactions American Geophysical*  
928 *Union*, 94(45), 409–410.
- 929 Wright, T. J., Elliott, J. R., Wang, H., & Ryder, I. (2013). Earthquake cycle defor-  
930 mation and the Moho: Implications for the rheology of continental lithosphere.  
931 *Tectonophysics*, 609, 504–523.
- 932 Yu, C., Li, Z., & Penna, N. T. (2018). Interferometric synthetic aperture radar  
933 atmospheric correction using a GPS-based iterative tropospheric decomposition  
934 model. *Remote Sensing of Environment*, 204, 109–121.
- 935 Yu, C., Li, Z., Penna, N. T., & Crippa, P. (2018). Generic atmospheric correction  
936 model for Interferometric Synthetic Aperture Radar observations. *Journal of*  
937 *Geophysical Research: Solid Earth*, 123(10), 9202–9222.
- 938 Yu, C., Penna, N. T., & Li, Z. (2017). Generation of real-time mode high-resolution  
939 water vapor fields from GPS observations. *Journal of Geophysical Research:*  
940 *Atmospheres*, 122(3), 2008–2025.
- 941 Zarifi, Z., Nilfouroushan, F., & Raeesi, M. (2014). Crustal stress map of Iran: In-  
942 sight from seismic and geodetic computations. *Pure and Applied Geophysics*,  
943 171(7), 1219–1236.
- 944 Zebker, H. A., Rosen, P. A., & Hensley, S. (1997). Atmospheric effects in interfer-  
945 ometric synthetic aperture radar surface deformation and topographic maps.  
946 *Journal of Geophysical Research: Solid Earth*, 102(B4), 7547–7563.

Figure 1.

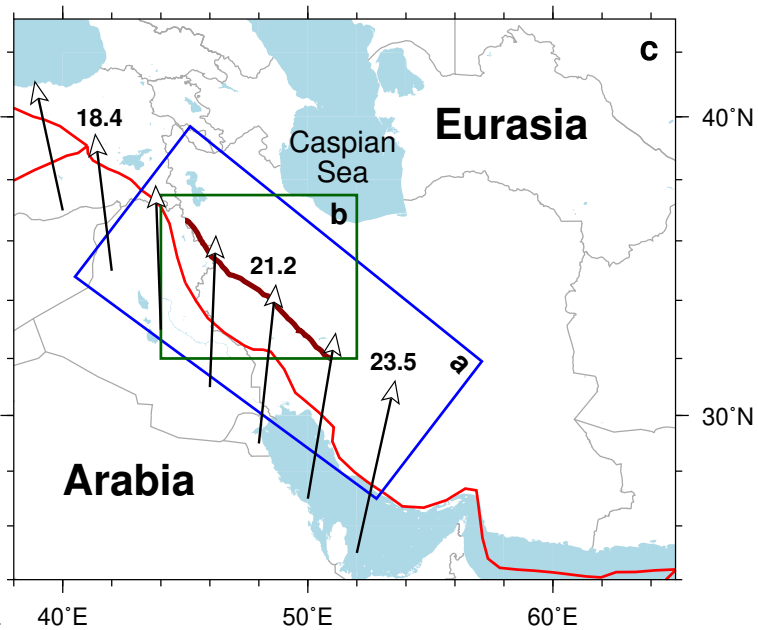
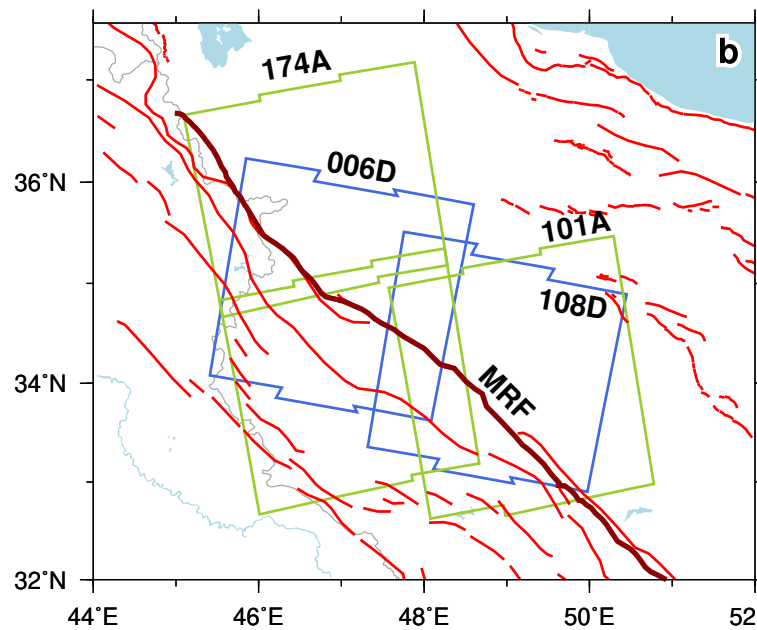
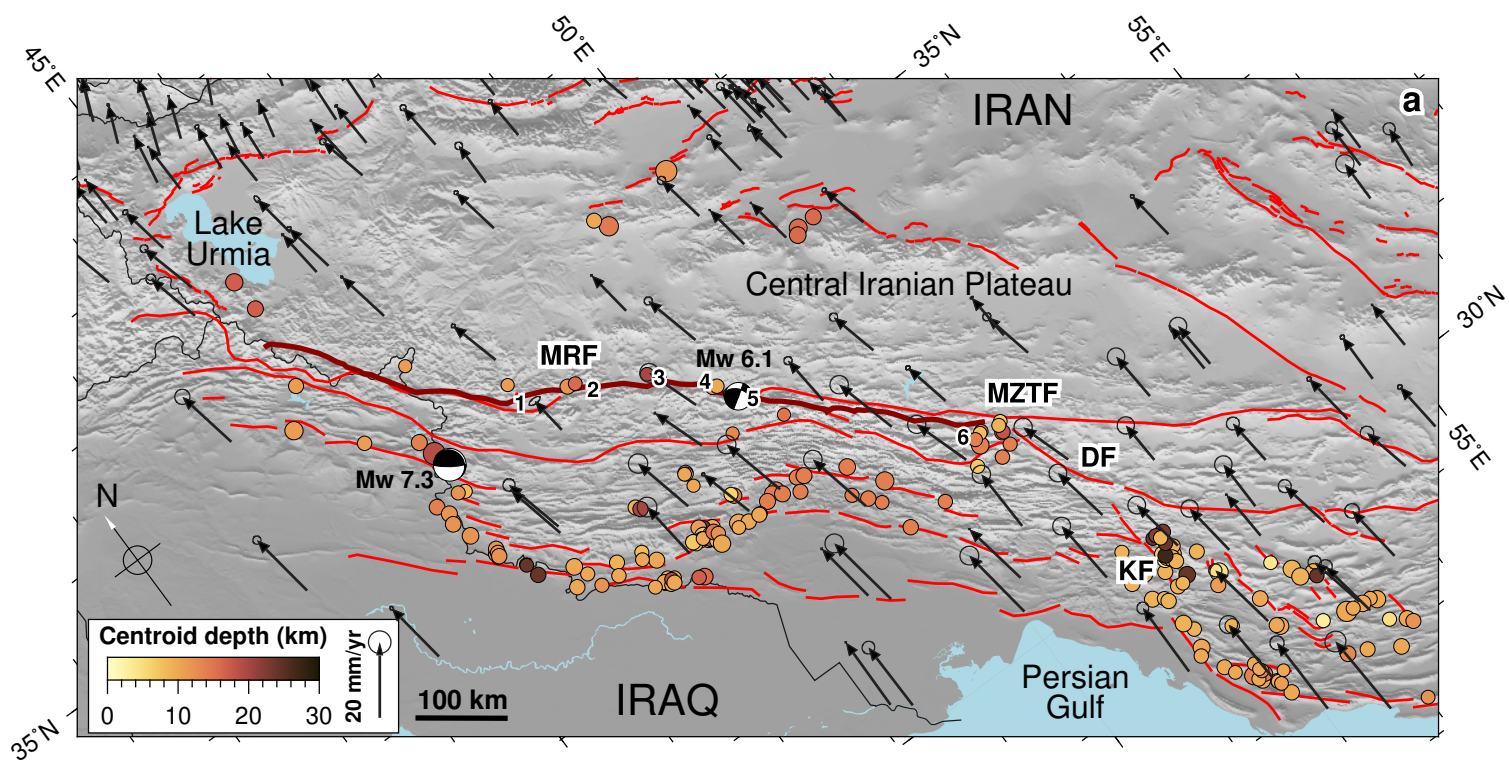


Figure 2.

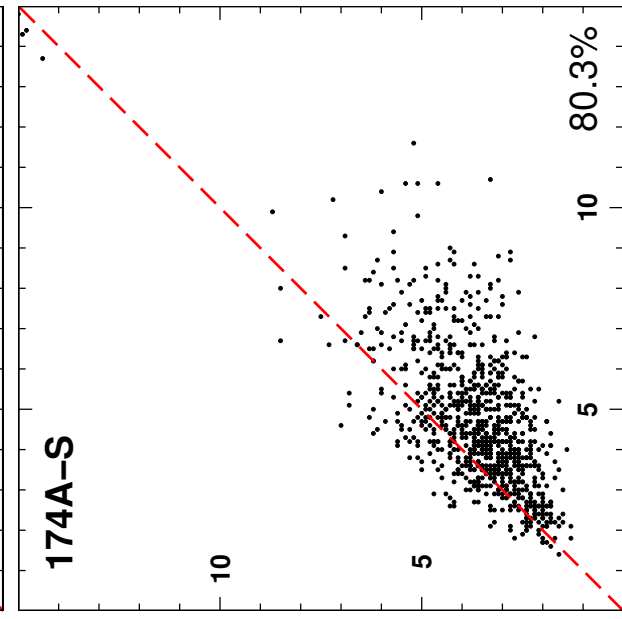
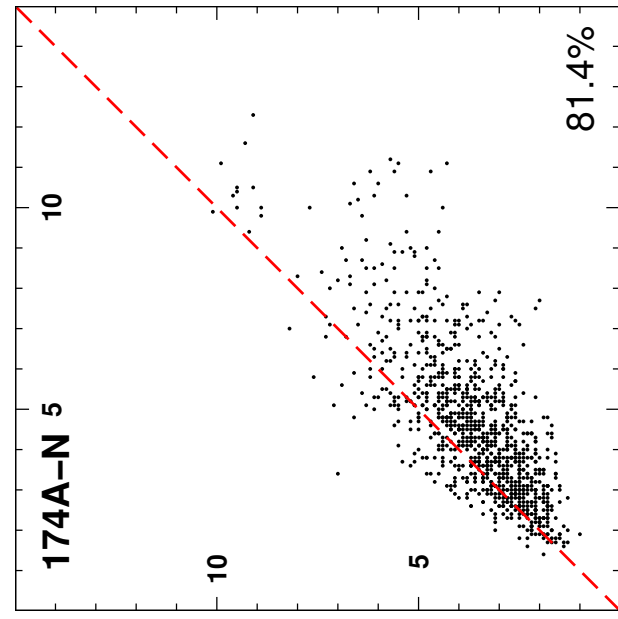
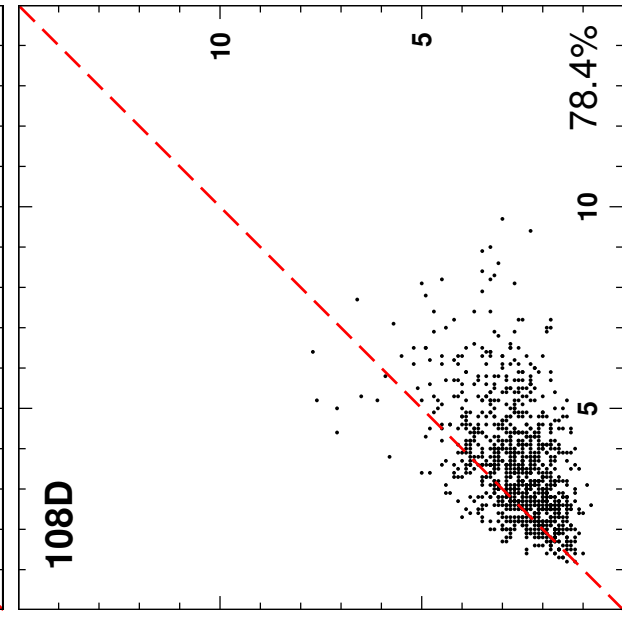
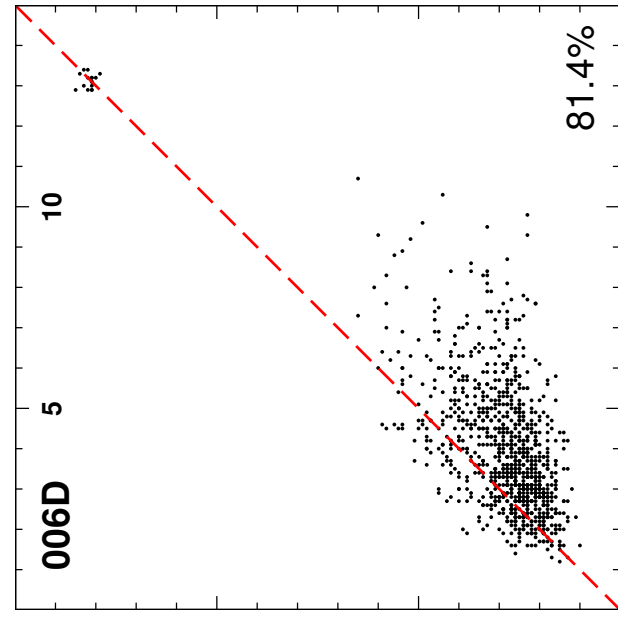
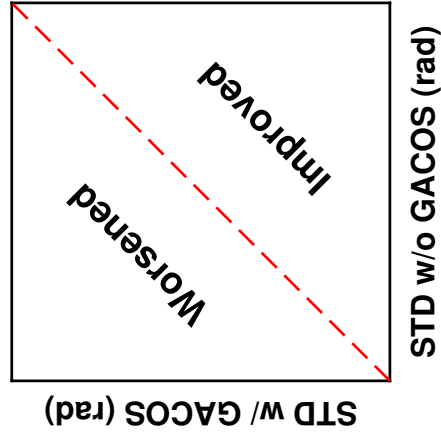
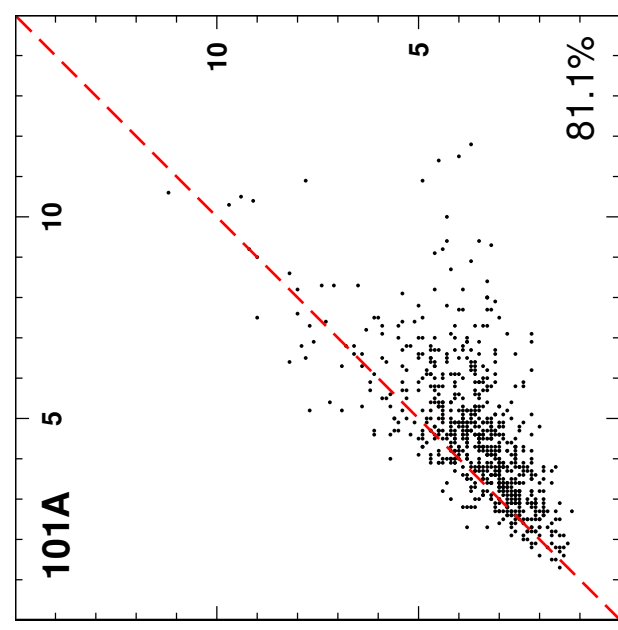
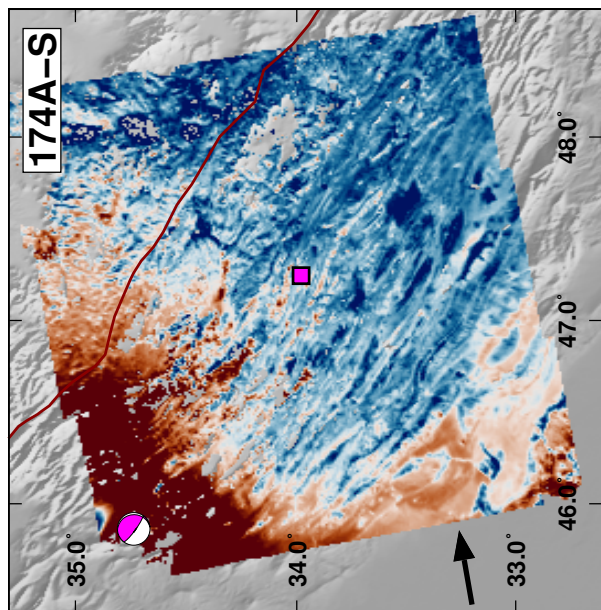
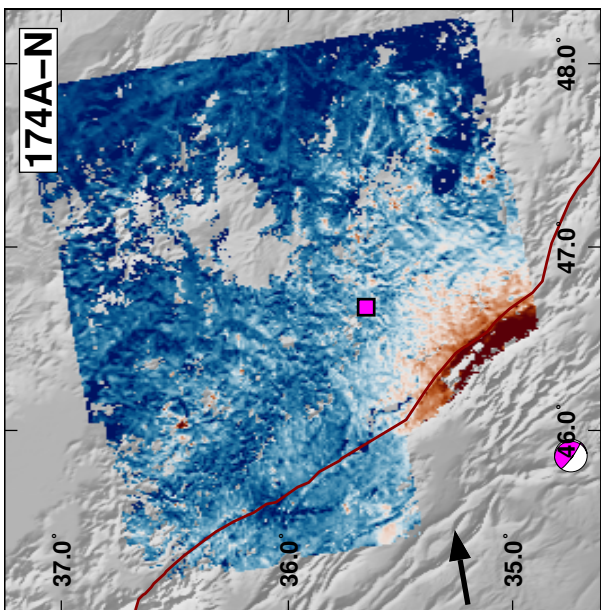
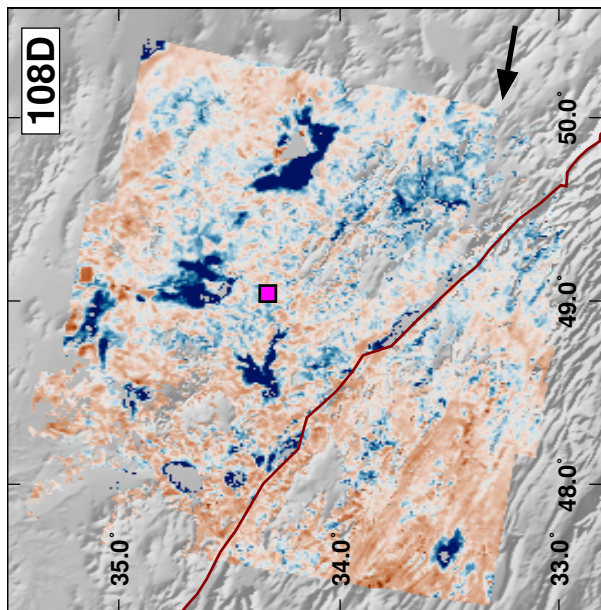
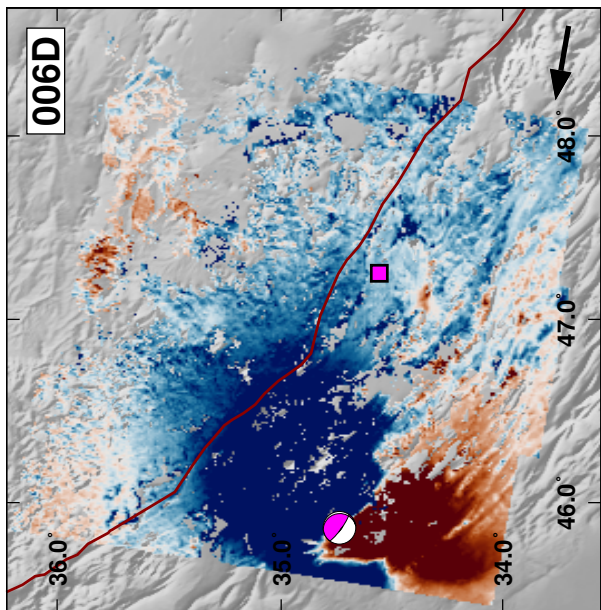
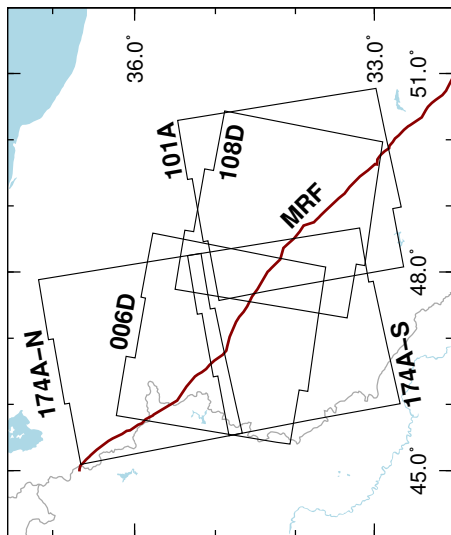
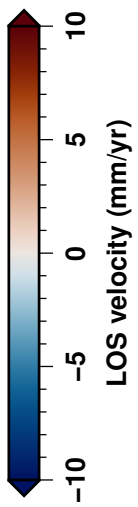
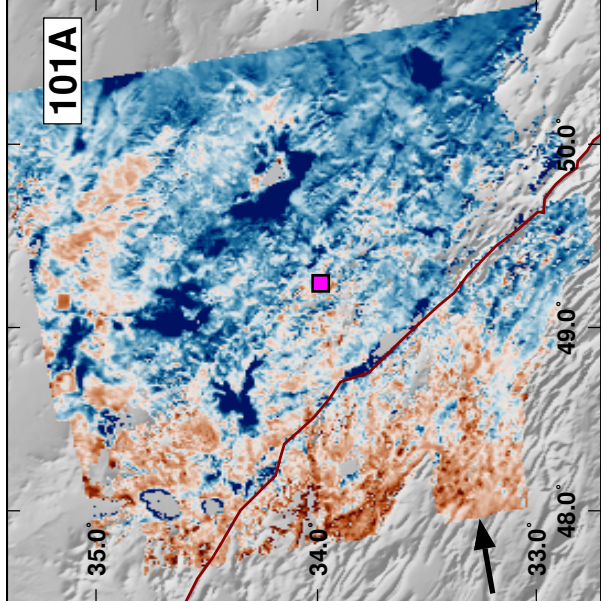


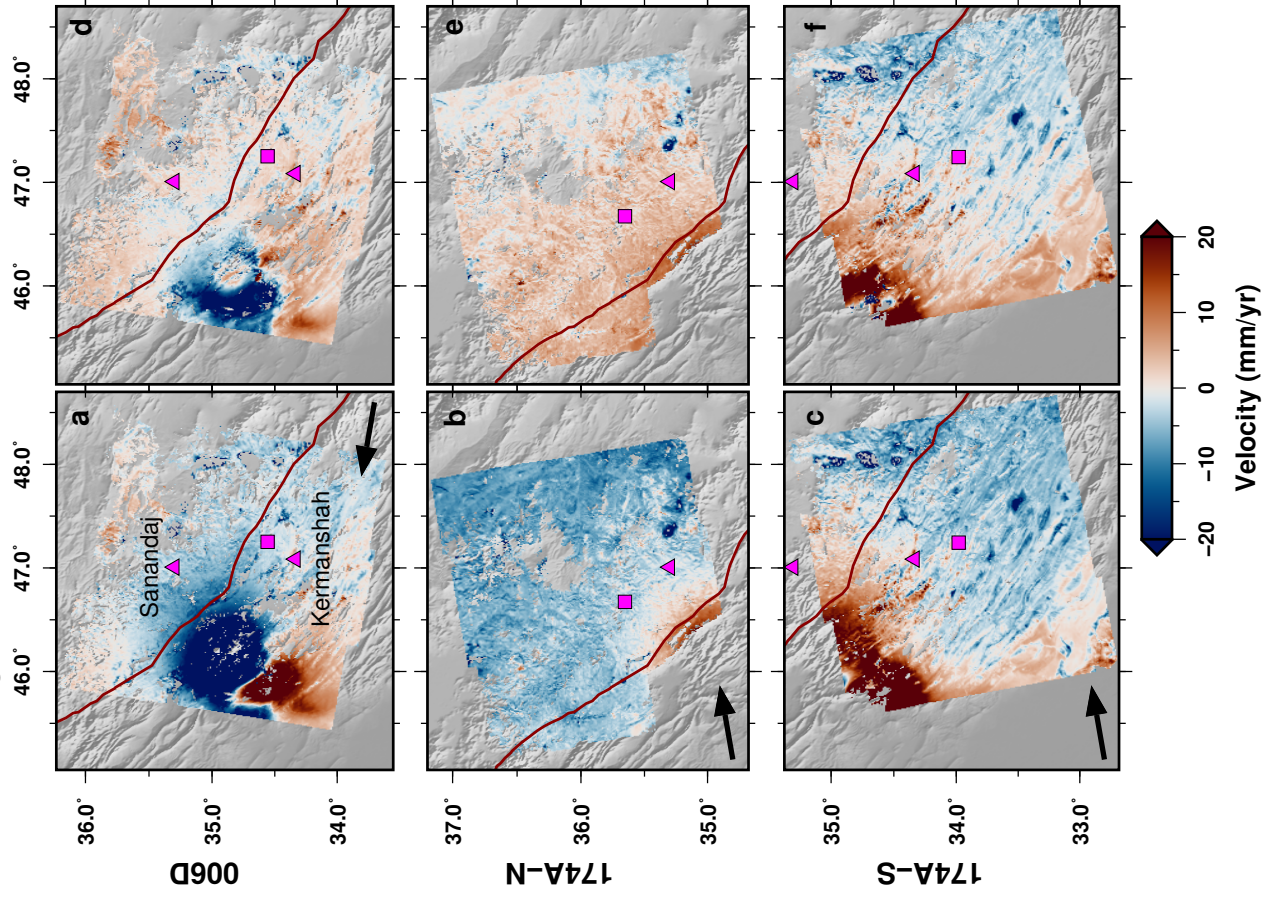
Figure 3.



**Figure 4.**

Original LOS velocities

Without co-seismic



Change in average line-of-sight velocity after the  $M_w$  7.3 Sarpol-e Zahab earthquake (12-11-2017)

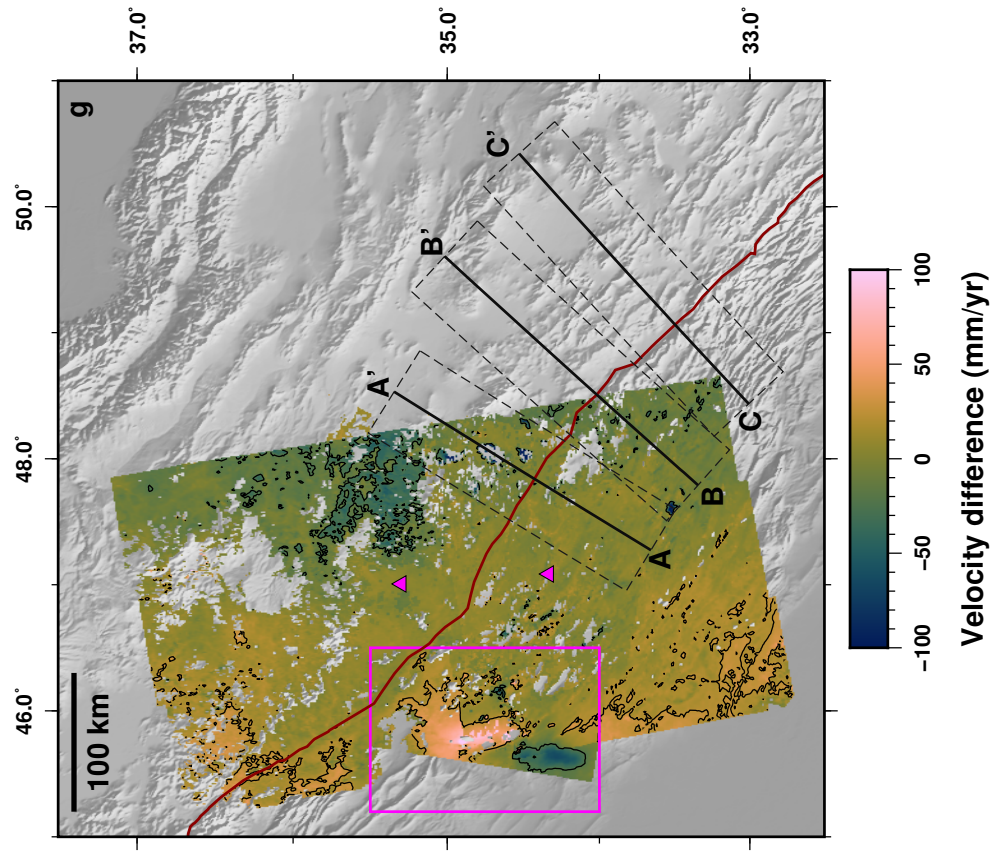


Figure 5.

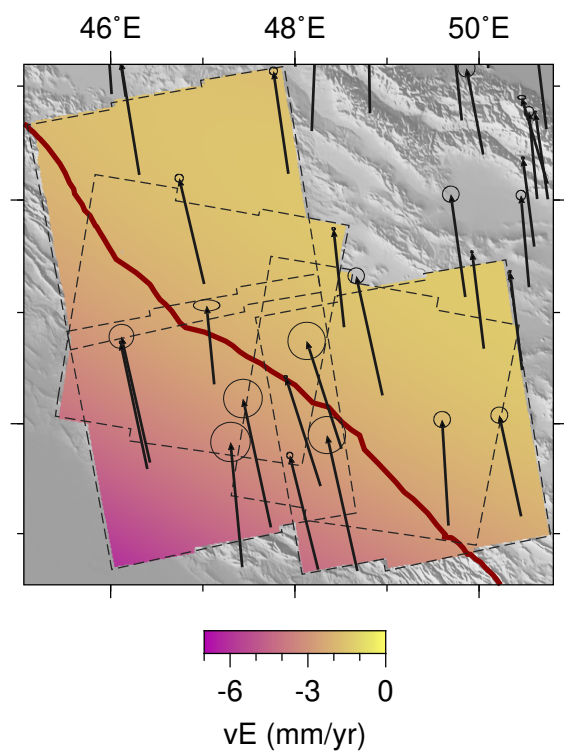
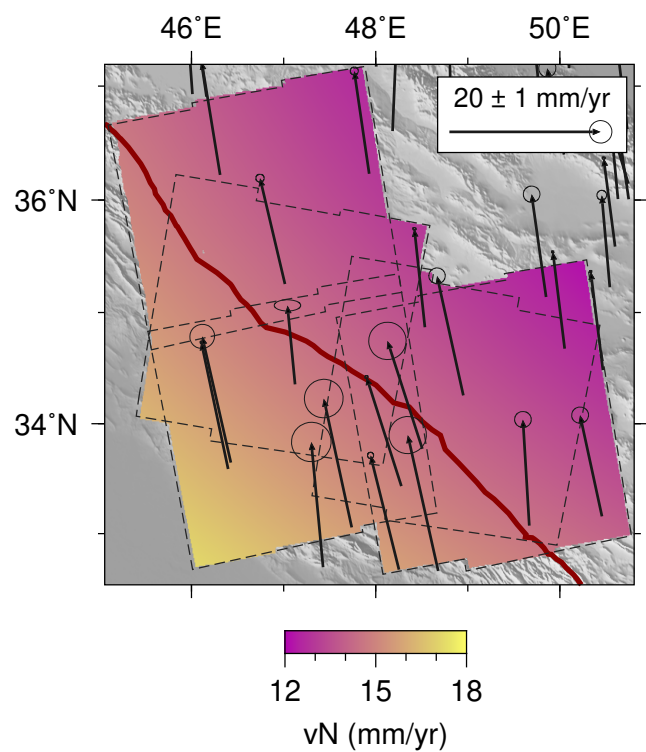


Figure 6.

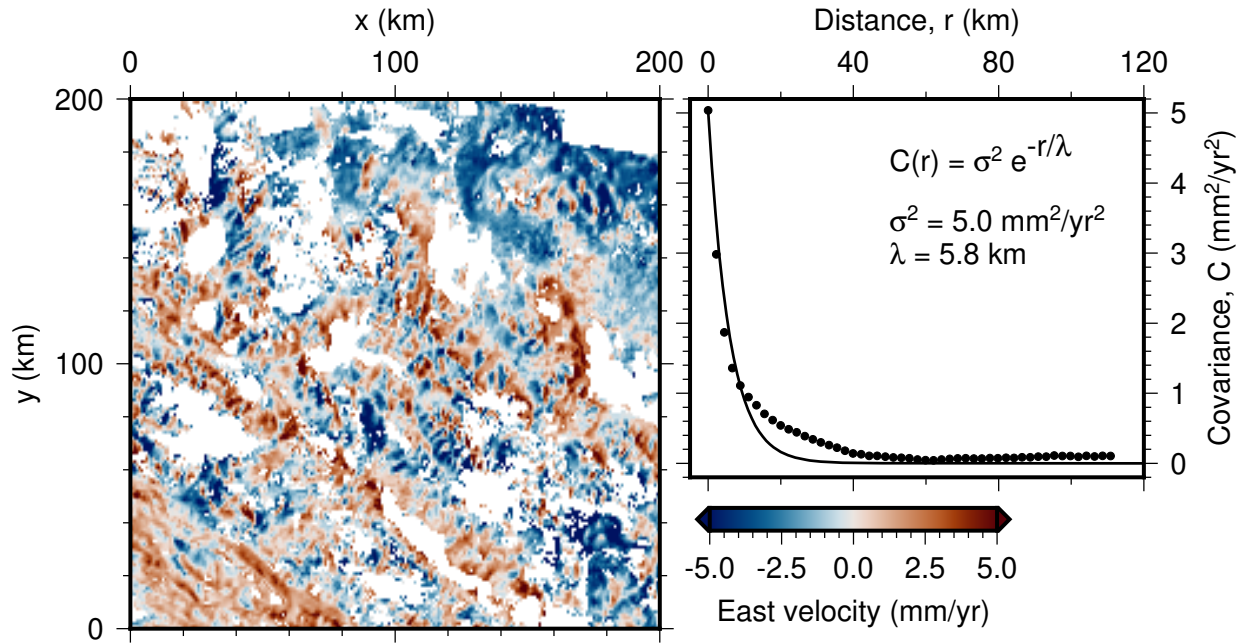


Figure 7.

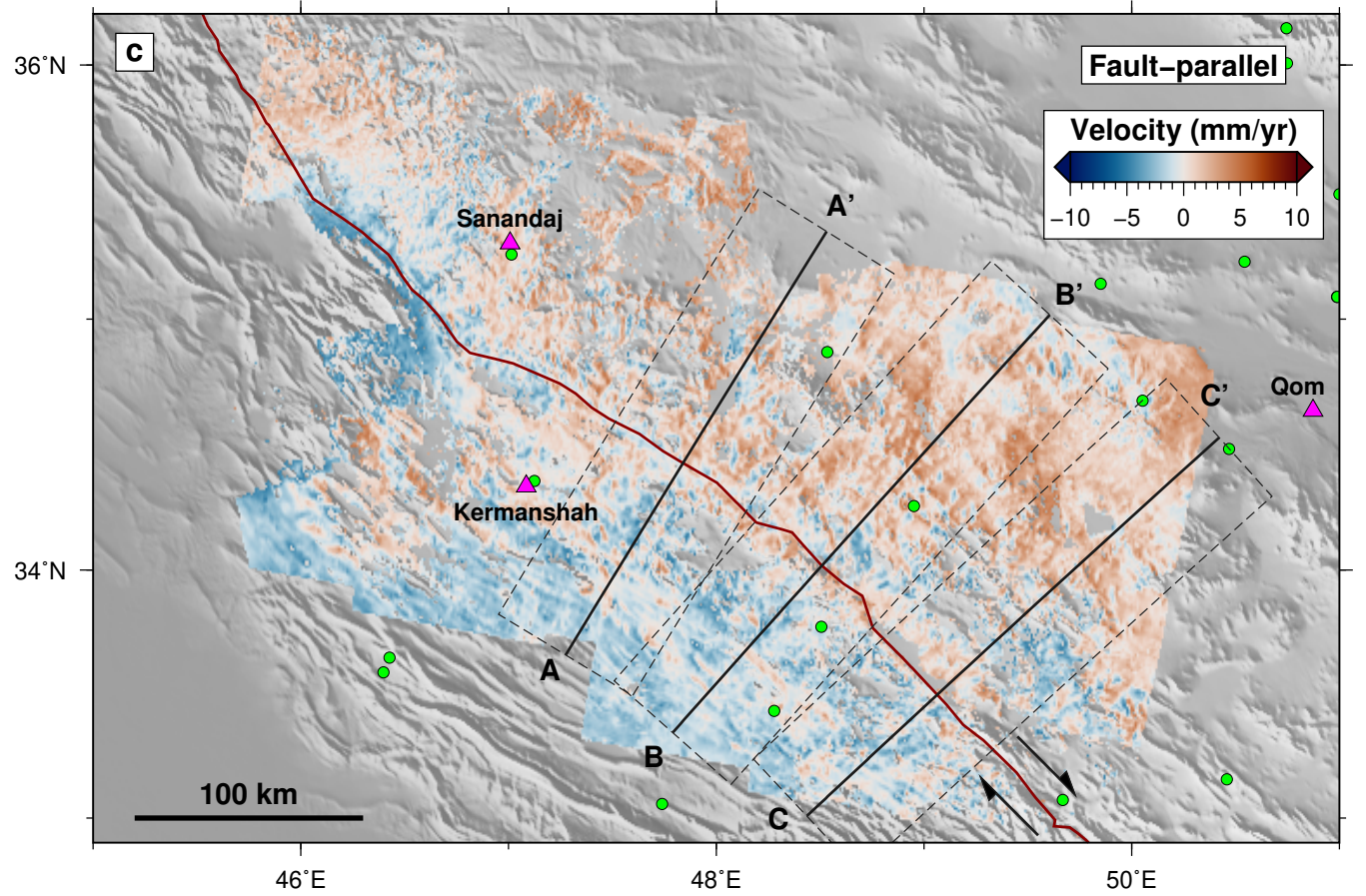
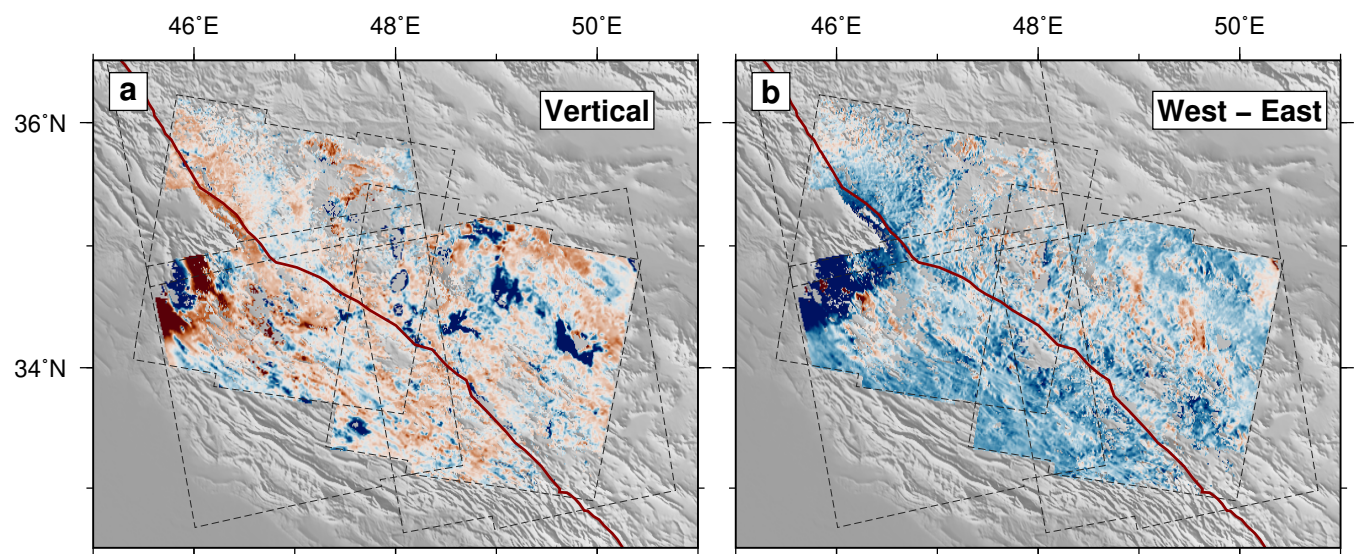


Figure 8.

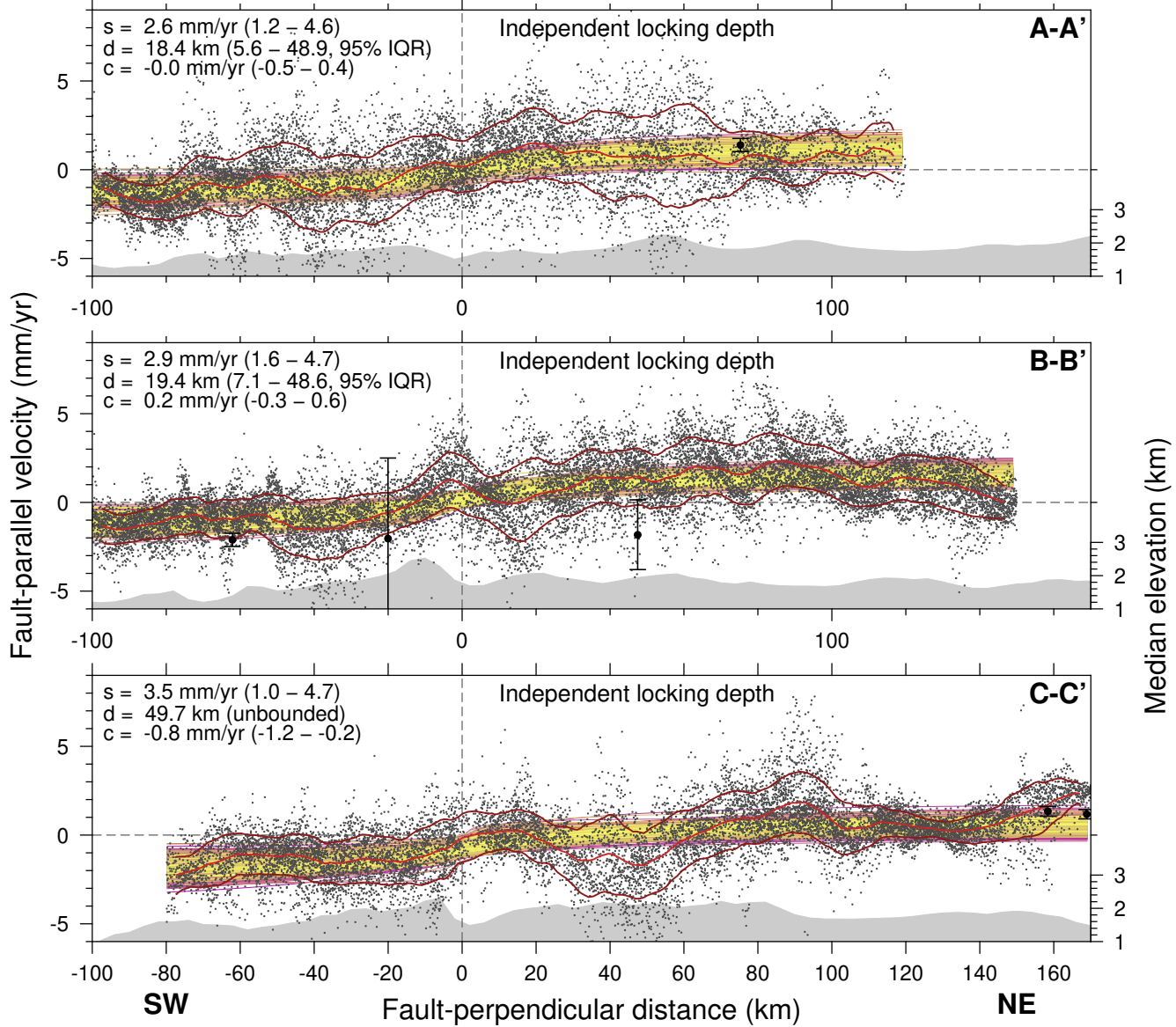


Figure 9.

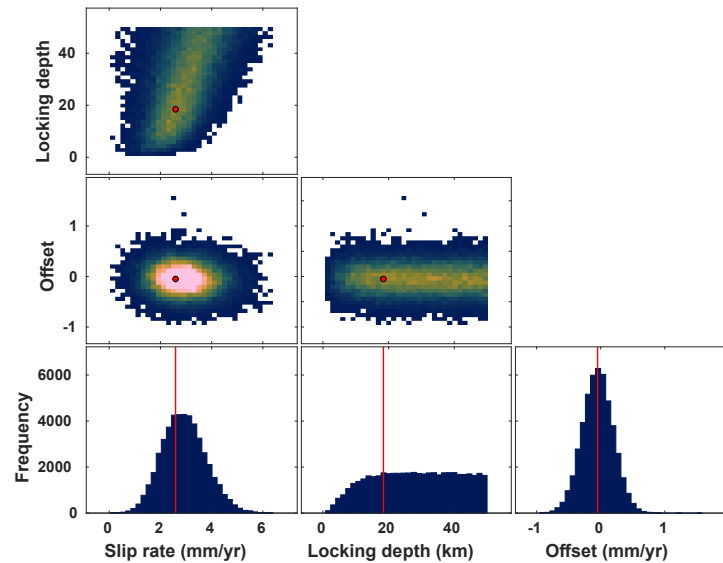
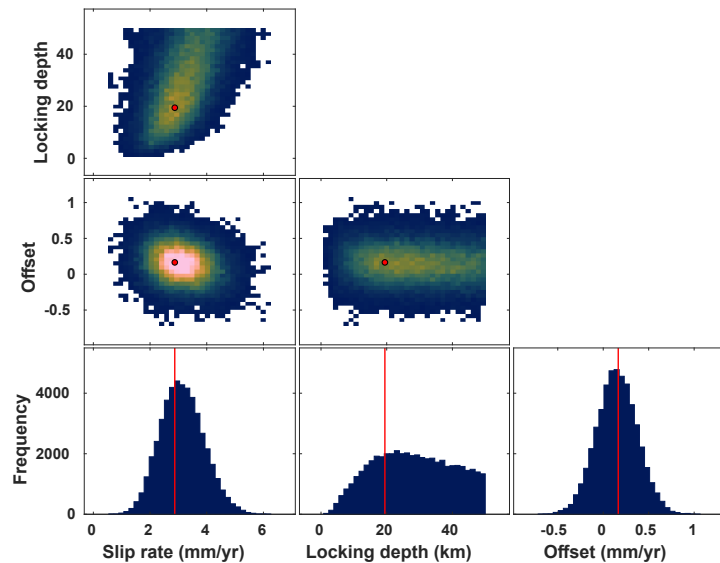
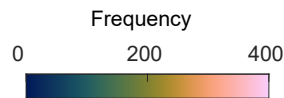
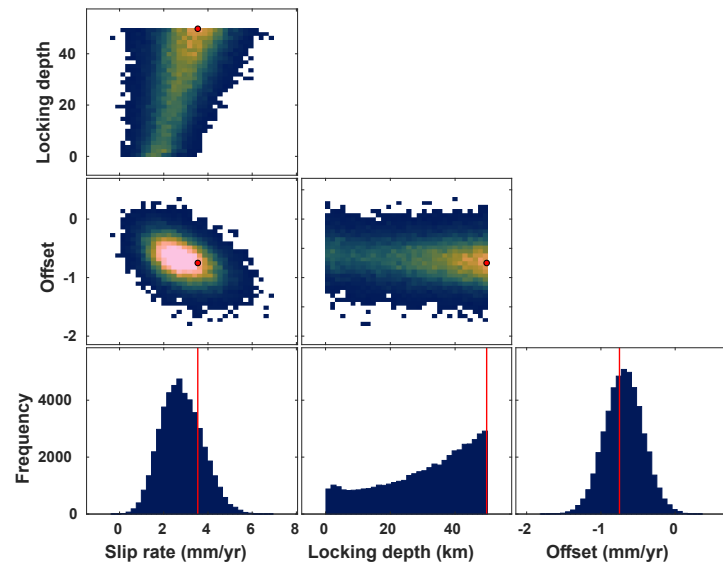
**A-A'****B-B'****C-C'**

Figure 10.

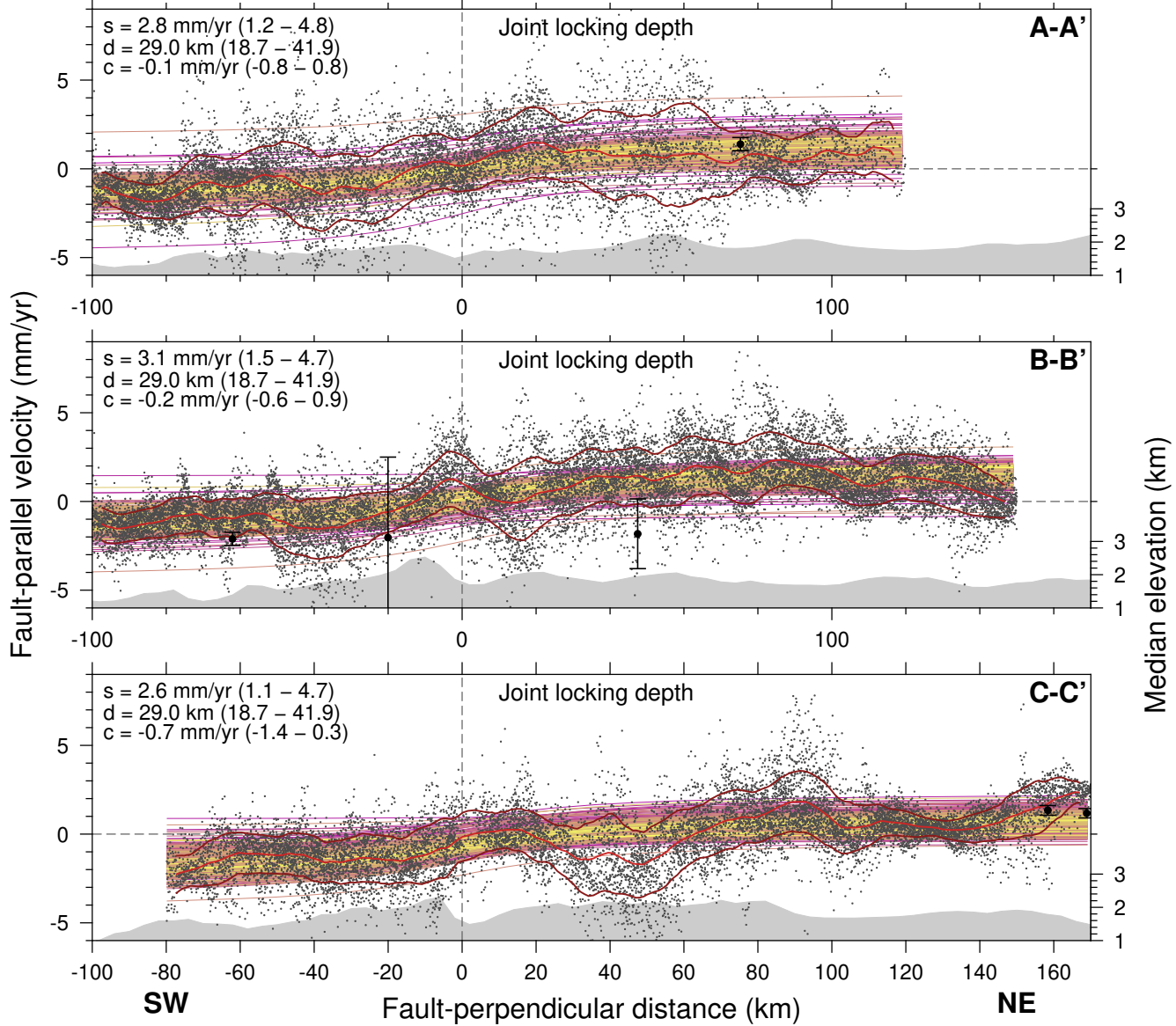


Figure 11.

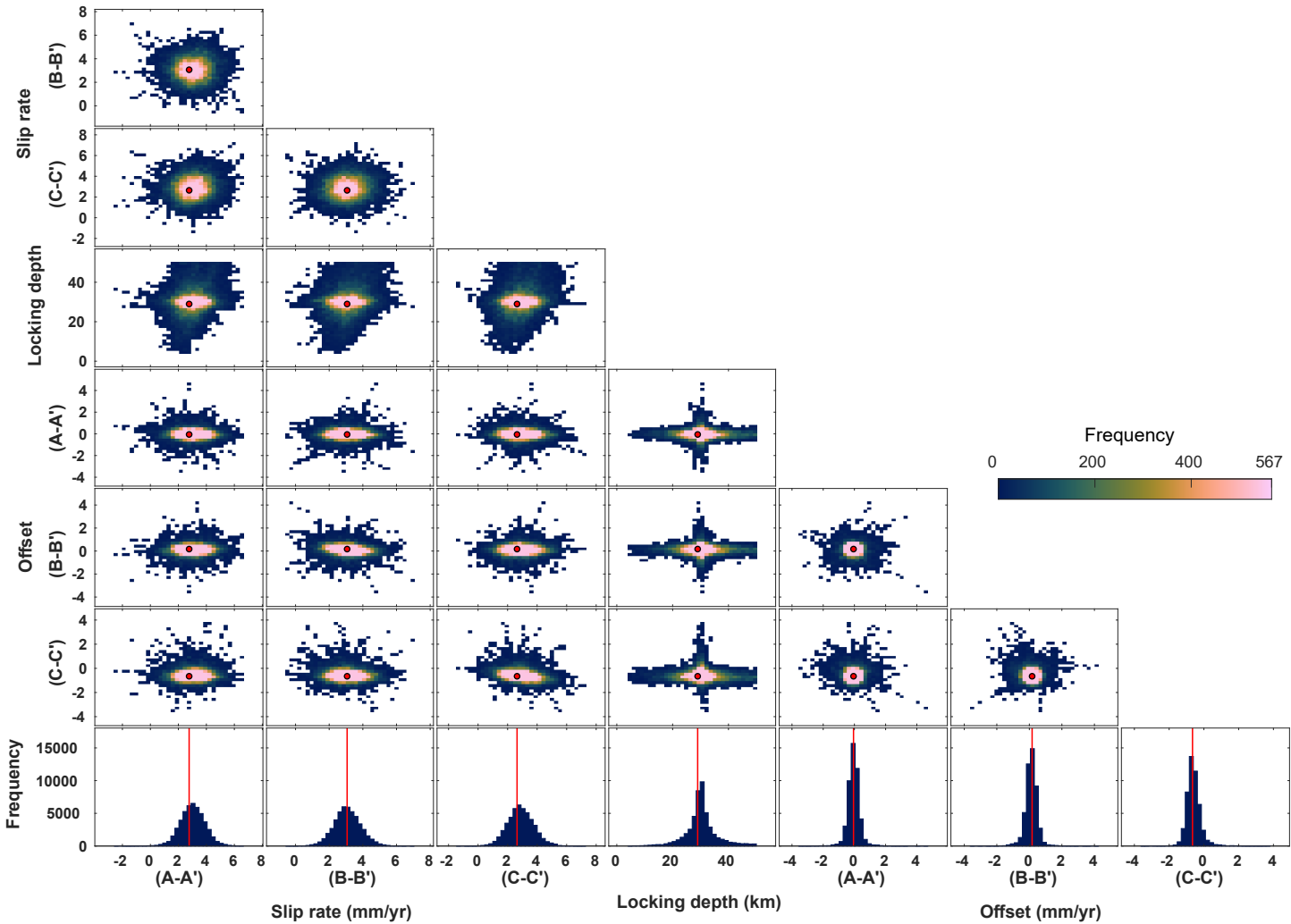


Figure 12.

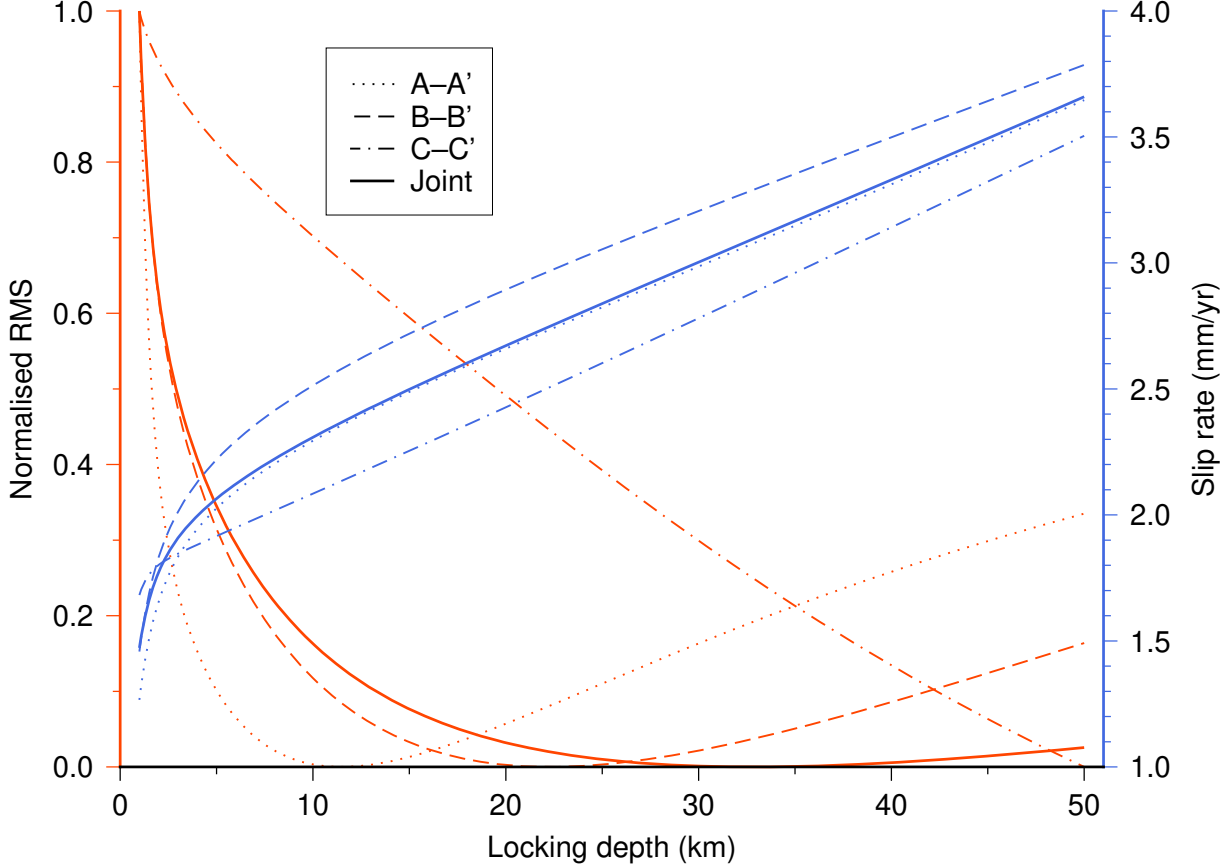
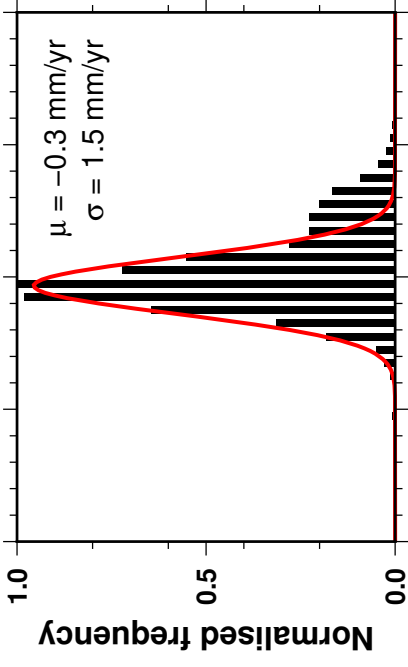
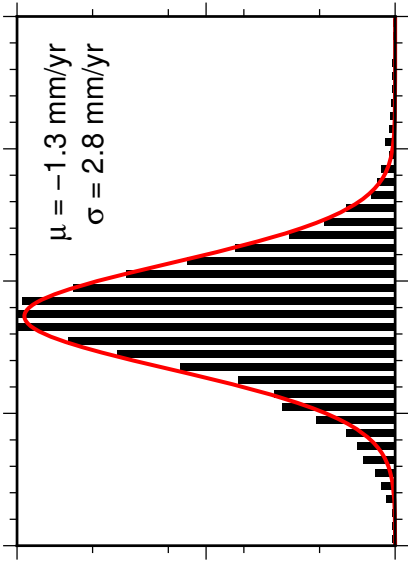


Figure 13.

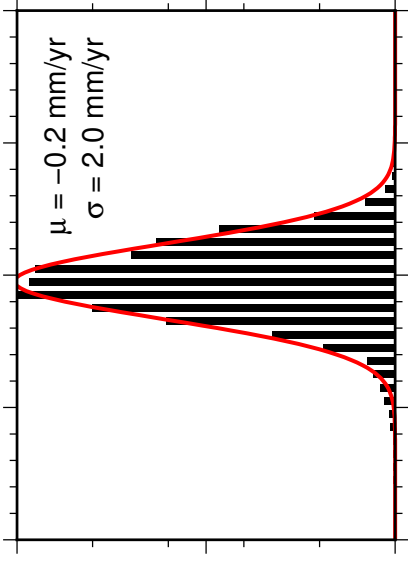
**Along-track ascending**



**Across-track ascending**



**Across-track descending**



Velocity difference (mm/yr)